Escape of hair follicle stem cells causes stem cell exhaustion during aging

Chi Zhang[1,6], Dongmei Wang[1,6], Jingjing Wang [1,6], Li Wang[2], Wenli Qiu[3], Tsutomu Kume [4], Robin Dowell[1,5] and Rui Yi [1,6] ✉

Stem cell (SC) exhaustion is a hallmark of aging. However, the process of SC depletion during aging has not been observed in live animals, and the underlying mechanism contributing to tissue deterioration remains obscure. We find that, in aged mice, epithelial cells escape from the hair follicle (HF) SC compartment to the dermis, contributing to HF miniaturization. Single-cell RNA-seq and assay for transposase-accessible chromatin using sequencing (ATAC-seq) reveal reduced expression of cell adhesion and extracellular matrix genes in aged HF-SCs, many of which are regulated by *Foxc1* and *Nfatc1*. Deletion of *Foxc1* and *Nfatc1* recapitulates HF miniaturization and causes hair loss. Live imaging captures individual epithelial cells migrating away from the SC compartment and HF disintegration. This study illuminates a hitherto unknown activity of epithelial cells escaping from their niche as a mechanism underlying SC reduction and tissue degeneration. Identification of homeless epithelial cells in aged tissues provides a new perspective for understanding aging-associated diseases.

Aging is defined as functional decline of tissues and organisms and contributes to many human diseases including cancer and neurodegenerative diseases[1,2]. Although it is widely recognized that SC exhaustion is a hallmark of aging[2], cellular activities of tissue SCs during aging have rarely been observed in their intact microenvironment[3,4]. It remains largely unknown how tissue SCs divide, migrate and perish during aging. Without a clear picture of these fundamental cellular behaviors, current knowledge of tissue SC aging has been acquired through indirect measurement of SC numbers and functions[5–10]. As a result, our understanding of SC exhaustion is largely limited to the deficiency of cell division and self-renewal, usually caused by DNA damage and cellular senescence[8,11–13].

Among fundamental properties of tissue SCs, quiescence is known to play an important role in SC maintenance by restricting the number of SC divisions and reducing cellular stress[14–17]. Although the loss of quiescence was shown to cause the lost proliferative potential of SCs in a cell-intrinsic manner[18,19], SC activities have not been visualized when they lose quiescence. Furthermore, it is unclear whether the loss of SC quiescence affects integrity of the SC compartment independently of cell-division control. Finally, SC division rates generally decrease during aging[20]; it remains an open question how prolonged SC quiescence affects aging.

The HF of mammalian skin is an excellent experimental system to examine cellular activities and molecular networks of largely quiescent SC populations during aging. HF loss and graying have been widely recognized as macroscopic signs of aging both scientifically and culturally. At the cellular level, HF miniaturization was reported to associate with hair loss during aging[8] and alopecia caused by premature hair loss[21,22]. In these studies, cell apoptosis as a result of accumulated DNA damage or altered signaling pathways, which are critical for hair growth, are identified as underlying mechanisms of SC exhaustion or compromised hair growth, respectively. However, HF-SCs and their activities have not been examined in live animals during aging.

In this study, we use noninvasive intravital imaging and single-cell genomic tools to measure multiple modalities of HF-SCs including cellular activities, the transcriptome and open-chromatin landscape in aged HFs. Surprisingly, we observe that numerous epithelial cells, many of them located near the bulge SC compartment, escape to the dermis during aging. We characterize the reduced expression of cell adhesion and extracellular matrix (ECM) genes as a prominent feature of aged HF-SCs and identify FOXC1 and NFATC1 as key regulators of HF-SC-specific cell adhesion. Deletion of the two corresponding genes recapitulates epithelial cell escape and leads to rapid HF miniaturization and hair loss. Our study reveals SC escape as a new mechanism for SC reduction and tissue degeneration.

Results

Escaped epithelial cells in aged HFs. To visualize the HF-SC compartment in live animals during aging, we used two-photon intravital imaging to observe histone H2B–green fluorescent protein (H2BGFP)-labeled (*Krt14*-H2BGFP) epithelial cells in HFs[23,24] in both young (~6–8-month (mo)-old) and old (>20-mo-old) mice. In young mice, the HF-SC compartment was readily distinguished by the convex morphology of the bulge region, which is located below the morphologically distinct sebaceous gland (SG), and epithelial cells were restricted within the cylinder of HFs regardless of hair cycle stages (Fig. 1a and Extended Data Fig. 1a). By contrast, miniaturized HFs, which are characterized by reduced cellularity, a shrinking bulge compartment and the upward movement of the HF-SC compartment toward SGs, were frequently observed in old mice (Fig. 1a). In some of these HFs, individual H2BGFP+ epithelial cells were located outside of the typical HF cylinder but in close proximity to the HF (Fig. 1a and Extended Data Fig. 1b). We also used second-harmonic-generation imaging of dermal collagen fiber

[1]Department of Molecular, Cellular and Developmental Biology, University of Colorado Boulder, Boulder, CO, USA. [2]10x Genomics, Pleasanton, CA, USA. [3]Lung Biology Center, Department of Medicine, UCSF, San Francisco, CA, USA. [4]Feinberg Cardiovascular and Renal Research Institute, Northwestern University Feinberg School of Medicine, Chicago, IL, USA. [5]BioFrontiers Institute, University of Colorado Boulder, Boulder, CO, USA. [6]Present address: Department of Pathology, Department of Dermatology, Northwestern University Feinberg School of Medicine, Chicago, IL, USA. ✉e-mail: yir@northwestern.edu
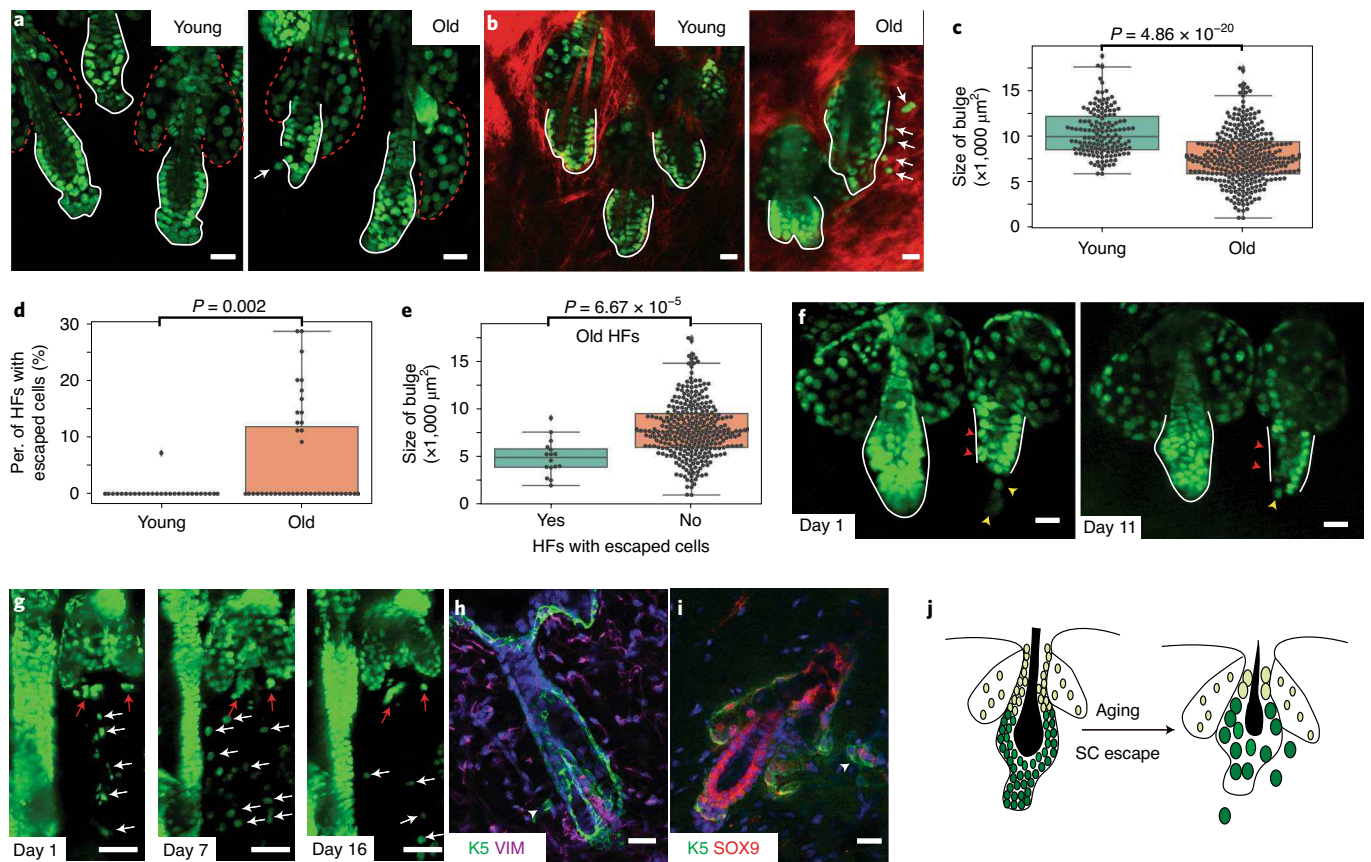
Fig. 1 | Aging HFs are characterized by escaped epithelial cells. a,b, Two-photon intravital imaging of young (P42) and old (20-mo) HFs. White arrows point to cells outside of the HF-SC compartment. Red dashed lines outline the SG. White lines outline the HF-SC compartment. Red signals in **b** are second-harmonic generation from collagen fiber in the dermis. Scale bar, 20 μm. **c**, Box plot of the size of the HF bulge region (mean ± s.d. = 10,423.62 ± 2,514.43 (young), 7,736.71 ± 2,913.99 (old); $n = 205$ HFs, five young mice; $n = 327$ HFs, three old mice). **d**, Box plot of the percentage (per.) of HFs containing escaped epithelial cells (mean ± s.d. = 0.25 ± 1.3 (young), 5.6 ± 8.9 (old); $n = 205$ HFs, five young mice; $n = 327$ HFs, three old mice). **e**, Box plot of the size of the HF bulge region, classified based on whether HFs contained escaped cells or not (mean ± s.d. = 4,933.35 ± 1,864.29 (escape), 7,883.78 ± 2,886.42 (no escape); $n = 327$ HFs, three old mice). Boxes span the first to the third quartile, with the line inside the box representing the median value. Whiskers show minimum and maximum values or values up to 1.5 times the interquartile range below or above the first or third quartile if outliers are present. Data are plotted as individual points and considered outliers beyond whiskers. Two-sided t-tests were performed for **c**–**e**. **f**, Longitudinal tracking of the same HFs in old mice (20 mo). Red arrowheads point to epithelial cells in the bulge region, which disappear during tracking. Yellow arrowheads point to escaped cells outside of the HF-SC compartment. White lines outline the bulge region. Scale bar, 20 μm. **g**, Longitudinal tracking of a rapidly miniaturized HF in an old mouse (20 mo). White arrows point to escaped epithelial cells in the dermis; red arrows point to the miniaturized HF. Scale bar, 50 μm. **h**, IF signals from an old HF (24 mo). The arrowhead points to a KRT5+ (K5) epithelial cell near the bulge region in the dermis. Scale bar, 20 μm. **i**, IF signals from an old HF (24 mo). The arrowhead points to KRT5+SOX9+ epithelial cells near the bulge region in the dermis. Scale bar, 20 μm. **j**, Illustration of HF aging accompanied by escaped cells.

and confirmed the localization of these H2BGFP+ epithelial cells in the dermis (Fig. 1b). We therefore refer to these cells as escaped epithelial cells.

We next quantified the size of the HF-SC compartment of telogen HFs in young and old mice. We observed a gradual but statistically significant reduction in the size of the HF-SC compartment in old mice (Fig. 1c). Overall, ~14.5% of the HF-SC compartment was miniaturized (defined by a size smaller than the smallest HF-SC compartment in young mice) in ~20-mo-old animals (Fig. 1c and Extended Data Fig. 1c). Furthermore, ~5.8% of aged HFs contained escaped H2BGFP+ epithelial cells near the HF-SC compartment (Fig. 1d). HFs with escaped epithelial cells were also significantly smaller than HFs without escaped cells (Fig. 1e). We have also examined apoptotic cells within the HF-SC compartment, which were previously shown to contribute to HF miniaturization[8]. On average, we observed that ~4.8% of aged HFs contained apoptotic HF-SCs marked by activated caspase 3 within the bulge region and

~4.8% within hair germs (HGs). We also observed that ~3.8% of young HFs contained apoptotic HF-SCs within the bulge region and ~5.8% within HGs (Extended Data Fig. 1d–f). These data suggest that the number of apoptotic cells, as detected by activated caspase 3, does not differ drastically in young and old mice.

To examine the relationship between epithelial cell escape and HF miniaturization, we longitudinally tracked the same HFs, which usually rested in the quiescent telogen phase, in live animals. In most frequently observed cases, we first observed signs of loosely organized epithelial cells in the bulge region, in contrast to the stereotypical morphology of the tightly packed HF-SC compartment in normal HFs. In ~10 d, these HFs lost some loosely organized epithelial cells and became smaller (Fig. 1f). In some rare but more rapidly progressing cases, we observed numerous H2BGFP+ epithelial cells scattering around miniaturizing HFs. Within a few days, these H2BGFP+ cells spread from the HF to neighboring regions or reached deeper regions of the dermis (Fig. 1g and Extended Data
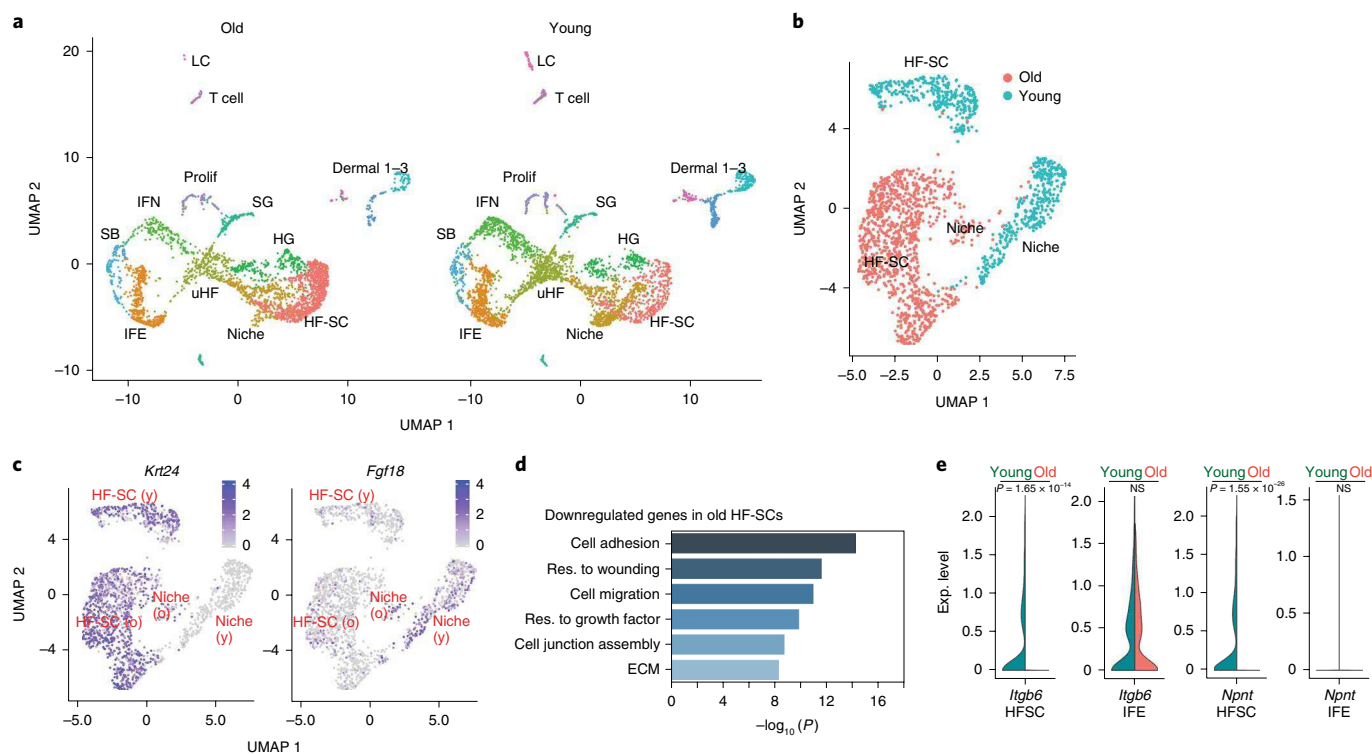
Fig. 2 | scRNA-seq reveals reduced cell adhesion in aged HF-SCs. a, UMAP clustering of skin cells from old (left) and young (right) mice. Major cell types are classified using marker genes and color coded with cell identity. uHF, upper HF region; IFN, infundibulum; dermal 1–3, three dermal populations; SB, suprabasal cells; prolif, proliferating cells; LC, Langerhans cells. **b**, UMAP reclustering of HF-SCs and niche cells in old and young mice. **c**, Feature plots of marker genes for HF-SCs (*Krt24*) and inner-bulge niche cells (*Fgf18*) in old (o) and young (y) samples. **d**, Highly enriched GO terms of downregulated genes in old HF-SCs. Res., response. **e**, Violin plots of selected cell adhesion and ECM genes in HF-SCs and IFE cells. Exp., expression; NS, not significant. Nonparametric Wilcoxon rank-sum tests were performed.

Fig. 1g). In about 2 weeks, however, most of these scattered cells were no longer visible, and the miniaturizing HF was rapidly degenerated (Fig. 1g). We further confirmed the epithelial identity of these scattered cells in the dermis as KRT5⁺VIM⁻ and KRT5⁺SOX9⁺ cells in aged mice (Fig. 1h,i and Supplementary Video 1). Escape of epithelial cells from the bulge to the dermis suggests compromised basement membrane (BM). Indeed, we observed HF-SCs in the bulge region protruding toward the dermis with immunofluorescence (IF) staining for β4 integrin, a BM marker, in old mice (Extended Data Fig. 1h). These data reveal an unexpected activity of epithelial cells escaping to the dermis in aged HFs and establish a correlation between epithelial cell escape and HF miniaturization during aging (Fig. 1j).

Reduced cell adhesion in aged HF-SCs. We next applied single-cell RNA-seq (scRNA-seq) to examine cellular states of skin epithelial cells isolated from young and old mice. HFs experience an increasingly long telogen phase and much less frequent anagen growth in old mice, and, by 18–24 mo, most HFs enter extended telogen, often lasting more than 100 d[25]. Therefore, we profiled the telogen phase as the representative hair cycle stage in young mice at postnatal day (P)53, the middle of the second telogen, and in old mice at 24 mo, which showed typical signs of aging such as hair thinning and occasionally gray hair. After quality control, we detected 3,524 epithelial cells in the P53 sample and 2,881 epithelial cells in the 24-mo sample (Extended Data Fig. 2a). We aggregated both young and old samples together and applied uniform manifold approximation and projection (UMAP) for dimension reduction to detect cell lineage dynamics and changes in the transcriptome[26]. Overall, three well-characterized, spatially distinct epithelial cell lineages,

including interfollicular epidermal (IFE) lineages, infundibular and SG lineages, and HF lineages were identified in both samples (Fig. 2a and Extended Data Fig. 2b,c). The projection of each lineage and individual cell clusters from young and old samples largely overlapped. To gain deeper insights into different cellular states at a higher resolution, we reclustered IFE and HF cells from young and old samples. Notably, epithelial cells in the HF-SC compartment from young mice were readily resolved into two distinct populations corresponding to outer-bulge HF-SCs and inner-bulge niche cells, marked by keratin (KRT)24 and fibroblast growth factor (FGF)18, respectively (Fig. 2b,c). By contrast, the demarcation of these two distinct populations was greatly reduced in the old sample (Fig. 2b,c), a trend similar to altered cellular states of fibroblasts during aging[27]. Interestingly, although basal cells of the IFE lineage showed different cellular states in young and old samples, differentiated suprabasal cells from young and old samples clustered together (Extended Data Fig. 3a–d).

We next performed differential gene expression analysis for HF-SCs and IFE basal cells between young and old samples. The most significantly downregulated genes in old HF-SCs were enriched for gene ontology (GO) terms such as regulation of cell adhesion, response to wounding, cell junction assembly and the ECM (Fig. 2d and Supplementary Table 1). Upregulated genes in old HF-SCs were enriched for the transcription factor (TF) AP1 complex and the apoptotic signaling pathway (Extended Data Fig. 3e and Supplementary Table 2). The most enriched GO categories in downregulated genes from old basal IFE progenitors were the major histocompatibility complex class I peptide-loading complex, response to wounding and negative regulation of cell differentiation (Extended Data Fig. 3f). The specificity of downregulated cell

adhesion and ECM genes in old HF-SCs was further supported by examining individual genes. For example, *Actg1* and *Itgb6* are widely expressed genes in both HF-SCs and IFE basal cells but were only downregulated in old HF-SCs and not in IFE cells (Fig. 2e and Extended Data Fig. 3g). *Npnt* (nephronectin (NPTN)), an HF-SC-specific ECM gene[28], was only detectable in HF-SCs and down-regulated in old samples (Fig. 2e and Extended Data Fig. 3g). By contrast, *Jun* and *Junb*, both encoding AP1 TFs, were upregulated in both HF-SCs and IFE cells from old mice.

We performed pseudotime analysis using Monocle 3 (ref. [29]) to examine lineage progression. It recapitulated the differentiation trajectory of distinct HF lineages in both young and old samples (Extended Data Fig. 3h). Interestingly, we observed a differential distribution of young and old HF-SCs along the pseudotime trajectory (Extended Data Fig. 3i). Young HF-SCs clustered in a more ground state, which was characterized by elevated gene expression in the adherens junction, tissue morphogenesis and regulation of cell adhesion. By contrast, many more old HF-SCs clustered in a more differentiated state, which was characterized by less cell adhesion (Extended Data Fig. 3j). These data reveal the reduction of cell adhesion and ECM gene expression specifically in aged HF-SCs.

Downregulation of *Foxc1* and *Nfatc1* in aged HF-SCs. To probe the transcriptional mechanism that underlies reduced gene expression during aging, we identified several enriched TF motifs in HF-SC-specific open-chromatin regions, determined by ATAC-seq, that surround downregulated genes in aged HF-SCs (Fig. 3a). Because aged HFs largely rest in extended telogen[25], the enrichment of ETS–RUNX motifs, which are generally associated with activated HF-SCs[30,31], was consistent with the lack of anagen HF growth. However, it was paradoxical that TFs promoting quiescence, including NFATC1, FOXC1 and TCF7L2 (refs. [7,10,32–34]), were associated with downregulated genes in largely quiescent HF-SC populations in aged mice. To examine this issue, we monitored the transcriptional activity of the *Foxc1* locus by using *Foxc1*-LacZ knock-in middle-aged mice (~15 mo old). In these mice, most HFs rested in telogen, but some HFs were still infrequently cycling and in anagen. We observed an absence of LacZ signals in quiescent HF-SCs located within the telogen bulge but robust LacZ signals in bulge regions of anagen HFs (Extended Data Fig. 4a–c). Furthermore, IF staining and quantification confirmed reduced expression of FOXC1 in aged HF-SCs located within the telogen bulge (Fig. 3b). Of note, *Foxc1* expression in the upper HF and SGs, determined by both *Foxc1*-LacZ and IF signals, was not changed (Fig. 3b and Extended Data Fig. 4), reflecting HF-SC-specific *Foxc1* downregulation. In addition, NFATC1 expression was also slightly downregulated in aged HF-SCs (Fig. 3c). We previously showed that *Foxc1* is induced in dividing HF-SCs during the anagen phase, and FOXC1 promotes the expression of *Nfatc1* and *Bmp2/6*[10]. Thus, the prolonged telogen diminishes expression of *Foxc1* in aged HF-SCs, likely due to the lack of anagen activation.

We next performed bulk RNA-seq to identify genes that are down-regulated in *Foxc1*-conditional knockout (cKO) (*Krt14-Cre/Foxc1*^{fl/fl})

and *Nfatc1*-cKO (*Krt14-Cre/Nfatc1*^{fl/fl}) HF-SCs, respectively. Interestingly, cell adhesion, the ECM and BM genes were top enriched GO categories for each cKO, in addition to well-appreciated regulation of signaling pathways such as BMP and FGF and the regulation of proliferation (Fig. 3d,e and Supplementary Tables 3 and 4). We further compared these downregulated genes to a published bulk RNA-seq dataset from aged HF-SCs[6] and identified a number of cell adhesion and ECM genes, such as *Ltbp1*, *Ccn2*, *Itgb6* and *Vwa2*, that were commonly downregulated in HF-SCs between aged mice and *Foxc1*- or *Nfatc1*-cKOs (Fig. 3f). Interestingly, we also identified genes prominently associated with HF-SC quiescence, such as *Peg3*, *Cd34*, *Fgf18*, *Nog* and *Tle4* (refs. [7,10,34–37]), that were commonly downregulated in aged and cKO HF-SCs (Supplementary Table 5). These downregulated cell adhesion and ECM genes harbored many open-chromatin regions containing FOXC1 and NFATC1 motifs within or near their loci (Fig. 3g). These data lend further support to a link between reduced *Foxc1* and *Nfatc1* expression and the aging of HF-SCs. Our analysis also reveals that extended quiescence of aged HF-SCs diminishes the expression of *Foxc1*.
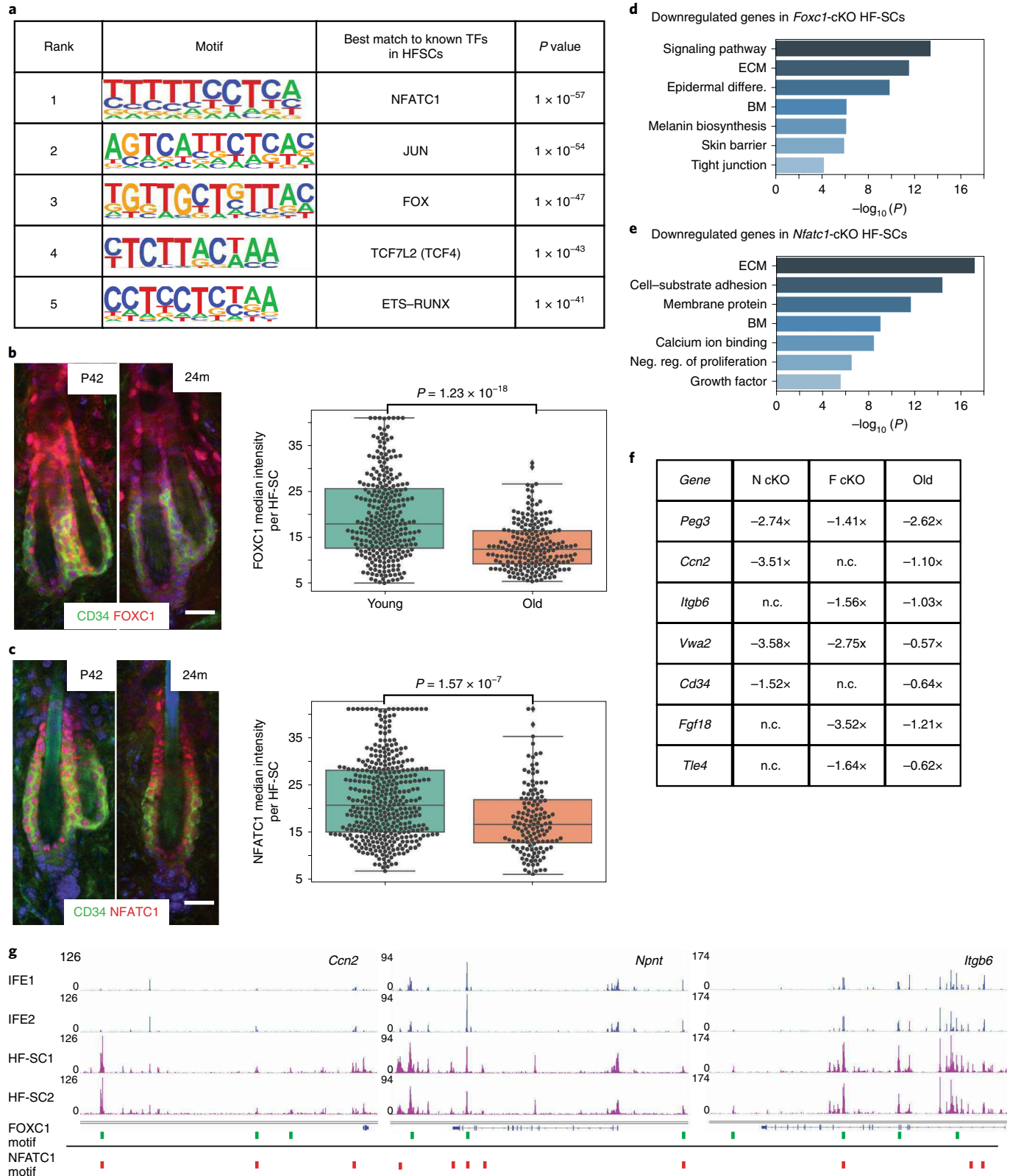
Loss of *Foxc1* and *Nfatc1* causes premature aging. To test the function of *Foxc1* and *Nfatc1* during aging, we deleted both TFs in the skin using *Krt14-Cre* (*Krt14-Cre/Foxc1*^{fl/fl};*Krt14-Cre/Nfatc1*^{fl/fl}), hereafter termed double knockout (dKO) mice (Fig. 4a). In young mice, we observed strongly compromised HF-SC quiescence as indicated by widespread Ki67 signals in HF-SCs in anagen I (P22), anagen III (P25) and the second telogen (P42) (Fig. 4b,c and Extended Data Fig. 5a). By contrast, HF-SCs in control animals were only in the active cell cycle transiently, mostly in early to middle anagen (Extended Data Fig. 5a), consistent with the notion that HF-SCs are largely quiescent and infrequently divide for self-renewal[38,39]. Furthermore, strong Ki67 signals were observed in the HF-SCs of dKO mice but not in those of *Foxc1*- or *Nfatc1*-single cKO mice by late anagen (Extended Data Fig. 5b), indicating a synergistic effect of deleting *Foxc1* and *Nfatc1* in quiescence control. At the tissue scale, young dKO mice rapidly regenerated their hair coat in less than 2 weeks after shaving, in sharp contrast to controls (Extended Data Fig. 5c).

Despite robust hair regeneration in young mice, dKO animals began to show signs of hair loss by ~5 mo of age (Fig. 4d). By 12–16 mo, dKO animals largely lost their hair coat, and the remaining hair turned gray, while they were otherwise healthy and had a normal lifespan (Fig. 4e and Extended Data Fig. 5d). We first examined whether compromised HF-SC quiescence led to loss of the proliferative potential of HF-SCs in dKO mice, as one may predict. However, we observed numerous Ki67+ proliferative cells in the HF-SC compartment of both growing and resting HFs in 16-mo-old dKO mice when hair loss was widespread (Fig. 4f). We then used intravital imaging to directly monitor dynamics of hair growth and loss in dKO animals. Strikingly, we observed many growing anagen HFs, which reflect robust HF growth, despite widespread hair loss. However, we also observed numerous miniaturized HFs

Fig. 3 | Downregulation of *Foxc1* and *Nfatc1* in aged HF-SCs. a, Top enriched TF motifs in HF-SC-specific open-chromatin regions surrounding downregulated genes in aged HF-SCs. Hypergeometric tests were performed. **b,c**, IF signals and quantification of FOXC1 and NFATC1 in CD34+ HF-SCs in young (P42) and 24-mo-old (24m) HFs. Scale bar, 20 μm. Representative images are from *n* = 5 young mice and *n* = 3 old mice. For FOXC1 signal intensity, mean ± s.d. = 1,957.39 ± 902.23 (young) and 1,312.08 ± 512.08 (old). For NFATC1 signal intensity, mean ± s.d. = 2,198.63 ± 845.53 (young) and 1,770.26 ± 718.86 (old). Boxes span the first to the third quartile, with the line inside the box representing the median value. Whiskers show minimum and maximum values or values up to 1.5 times the interquartile range below or above the first or third quartile if outliers are present. Data are plotted as individual points and considered outliers beyond whiskers. Two-sided *t*-tests were performed. **d,e**, Highly enriched GO terms of downregulated genes in *Foxc1*-cKO HF-SCs (**d**) and *Nfatc1*-cKO HF-SCs (**e**). Results from hypergeometric tests with Benjamini–Hochberg *P* values are shown. Differe., differentiation; neg., negative; reg., regulation. **f**, HF-SC-enriched cell adhesion and ECM genes and their expression change in each cKO strain and old mice. N cKO, *Nfatc1* cKO; F cKO, *Foxc1* cKO; n.c., no change. Wald tests were performed; statistical values are shown in Supplementary Table 5. **g**, ATAC-seq tracks of *Ccn2*, *Npnt* and *Itgb6* loci in IFE cells and HF-SCs, annotated with FOXC1 (green marks) and NFATC1 (red marks) motifs. ATAC-seq data are normalized and displayed at the same scale across all samples.

concurrently in the same dKO animals. Some HFs were reduced to a few remaining cells and progressed toward complete degeneration (Fig. 4g and Extended Data Fig. 5e). Unlike control HFs that typically clustered together with 2–4 HFs, which were usually in telogen, dKO HFs had irregular spacing, indicative of widespread but random HF loss as observed at the macroscopic level.

By examining the morphology of miniaturizing HFs, we found that many H2BGFP+ epithelial cells were located in the vicinity of the HF-SC compartment but were clearly outside of the HF cylinder (Fig. 4g and Extended Data Fig. 5e), recapitulating escaping epithelial cells as observed in aged HFs (Fig. 1). We next quantified the size of the telogen HF-SC compartment, the percentage of minia-

a

Rank	Motif	Best match to known TFs in HFSCs	P value
1		NFATC1	1×10^{-57}
2		JUN	1×10^{-54}
3		FOX	1×10^{-47}
4		TCF7L2 (TCF4)	1×10^{-43}
5		ETS–RUNX	1×10^{-41}

b

CD34 FOXC1

$P = 1.23 \times 10^{-18}$

FOXC1 median intensity per HF-SC: Young, Old

c

CD34 NFATC1

$P = 1.57 \times 10^{-7}$

NFATC1 median intensity per HF-SC: Young, Old

d Downregulated genes in *Foxc1*-cKO HF-SCs

Signaling pathway, ECM, Epidermal differe., BM, Melanin biosynthesis, Skin barrier, Tight junction

$-\log_{10}(P)$

e Downregulated genes in *Nfatc1*-cKO HF-SCs

ECM, Cell–substrate adhesion, Membrane protein, BM, Calcium ion binding, Neg. reg. of proliferation, Growth factor

$-\log_{10}(P)$

f

Gene	N cKO	F cKO	Old
Peg3	−2.74×	−1.41×	−2.62×
Ccn2	−3.51×	n.c.	−1.10×
Itgb6	n.c.	−1.56×	−1.03×
Vwa2	−3.58×	−2.75x	−0.57×
Cd34	−1.52×	n.c.	−0.64×
Fgf18	n.c.	−3.52×	−1.21×
Tle4	n.c.	−1.64×	−0.62×

g

IFE1, IFE2, HF-SC1, HF-SC2, FOXC1 motif, NFATC1 motif

Ccn2, Npnt, Itgb6

turized HFs and the percentage of HFs containing escaped epithelial cells in dKO mice and compared to these data to those from young and aged mice (Fig. 4h,i and Extended Data Fig. 5f). On average, 12-mo-old dKO mice had 4.3-fold more (77.3% versus 14.5%) miniaturized HFs than 20–24-mo-old mice. The percentage of HFs containing escaped epithelial cells was 10.5% in dKO mice and 5.8% in aged mice. These results were consistent with the rapid progression of hair loss and premature HF aging observed in dKO mice.

To monitor the process of HF degeneration in live animals, we longitudinally tracked the same HFs in dKO mice for multiple weeks. We observed that HF miniaturization and degeneration occurred invariably after the catagen-to-telogen transition. Notably, rather than forming the anatomically distinct bulge, miniaturizing HFs in dKO mice first showed signs of abnormal cell egress in the bulge region (day 3 in Fig. 4j and Supplementary Video 2). These escaping cells were transient and were not observed at day 1 or 5 or any time points other than day 3. The HF then regressed to a loosely packed epithelial strand, which lacked convex morphology (day 9 in Fig. 4j), mimicking many miniaturized HFs observed in aged skin. In ~3 weeks, these dKO HFs became further miniaturized until complete degeneration with less than five cells left in the HF (day 26 in Fig. 4j). To determine the correlation between HF miniaturization and the number of HF-SCs, we quantified the number of HF-SCs in telogen HFs directly in live animals. The number of HF-SCs per HF was significantly reduced in old mice and even more so in dKO mice (Extended Data Fig. 5g,h).

In addition to these rapidly dying HFs, however, we also observed many HFs that went through the hair cycle and continuously regenerated in the same animals (Extended Data Fig. 5i). Notably, these HFs did not shown signs of epithelial cell escape and continued to cycle within our observation window. Thus, the appearance of escaping epithelial cells from the bulge region distinguished miniaturizing HFs from continuously cycling HFs in dKO mice. Overall, we have tracked 78 individual HFs over the span of at least 16 d. We found that 62.8% of HFs underwent regeneration, 26.9% underwent miniaturization and degeneration and 9.0% remained quiescence (Extended Data Fig. 5j).

These live imaging data reveal the dynamics of HF-SC loss accompanying by HF miniaturization. They suggest that the loss of HF-SCs through cell escape rather than enhanced HF-SC proliferation or compromised proliferative potential is correlated with SC exhaustion in dKO mice.

Reduced expression of cell adhesion and ECM genes. We next performed scRNA-seq to examine changes in gene expression in control and dKO samples at P38, when HFs are in late anagen and HF-SCs return to quiescence[10]. Similar to aged skin, cell clusters of epithelial cell populations did not change drastically, judging by the UMAP projection (Fig. 5a and Extended Data Fig. 6a–c). Notably,

genes involved in the regulation of cell adhesion and negative regulation of cell proliferation were among the most enriched among downregulated genes in dKO HF-SCs (Fig. 5b and Supplementary Table 6). Among these genes, many are commonly downregulated in aged HF-SCs such as *Actg1*, *Cd34*, *Itgb6* and *Npnt*.

To examine the specificity of *Foxc1*- and *Nfatc1*-mediated regulation in HF-SCs, we used *Krt15-CrePR* to delete *Foxc1* and *Nfatc1* only in the HF-SC compartment starting at P22 (Extended Data Fig. 7a) and purified dKO HF-SCs for bulk RNA-seq at P30. In support of the notion that these two TFs govern HF-SC gene expression in a cell-intrinsic manner, a large number of genes, which were downregulated in *Foxc1*- and *Nfatc1*-single cKO mice, were also downregulated in induced dKO mice (Fig. 5c,d and Supplementary Table 7). Because both TFs were only deleted in induced dKO mice shortly before sample collection, nearly all of these genes were more mildly downregulated in induced dKO mice than those in either single cKO strain, in which each TF was deleted at the beginning of skin development with *Krt14-Cre* (Fig. 5d). Consistent with scRNA-seq data, the most highly enriched gene categories that were downregulated in induced dKO HF-SCs were cell adhesion, negative regulation of cell proliferation and ECM genes (Fig. 5e). Among cell adhesion and ECM genes that were downregulated, *Igfbp5*, *Ccn2*, *Postn*, *Ltbp2*, *Col6a1*, *Npnt* and *Egfl6* are highly enriched in HF-SCs[28]. Among upregulated genes, the strongest elevation of gene expression was associated with mitotic cell cycle and cytokinesis in dKO HF-SCs (Extended Data Fig. 7b).

We next examined the expression of several cell adhesion and ECM genes including *Npnt*, *Cd34* and *Egfl6* in dKO and aged animals. At P42, when dKO HFs were morphologically in the telogen phase, NPNT, CD34 and epidermal growth factor-like domain (EGFL)6 signals were all significantly reduced. In particular, CD34 was not detectable (Fig. 5f). In 24-mo-old samples, NPNT and CD34 signals but not EGFL6 signals were also reduced (Fig. 5f,g). Interestingly, the expression of NPNT, an ECM protein that is localized to the BM of the bulge and HGs[28], was lost specifically in bulge HF-SCs but not in HGs of both dKO and old samples (Fig. 5f), further supporting HF-SC-specific control of *Npnt* by FOXC1 and NFATC1. We next confirmed that CD34 was absent in *Krt14-Cre/Foxc1*fl/fl;*Krt14-Cre/Nfatc1*fl/fl dKO HF-SCs at P30 by using flow cytometry (Extended Data Fig. 7c,d). By comparison, CD34 was expressed at a lower but still detectable level in both *Foxc1*- and *Nfatc1*-single cKO HF-SCs (Extended Data Fig. 7e). Furthermore, in *Krt15-CrePR*-induced dKO mice, CD34 levels were also downregulated but not completely lost 8 d after induction of deletion (Extended Data Fig. 7f). These data suggest that *Cd34*, encoding one of the most specific HF-SC surface markers and a cell adhesion gene[40–42], requires the combinatorial control of these two TFs (also see below). Despite the complete loss of CD34, however, dKO HF-SCs still maintained their fate as indicated by the robust expression

---

Fig. 4 | Genetic deletion of *Foxc1* and *Nfatc1* causes premature hair loss. a, IF signals of FOXC1 and NFATC1 expression in the HF-SC compartment at late anagen (left, marked by CD34) and early telogen (middle, marked by KRT15) and in dKO mice (right, marked by KRT15). Scale bar, 20 μm. Ctrl, control. **b,c**, Staining and quantification of Ki67+ cells in the HF-SC compartment in early anagen (**b**) and early telogen (**c**). White arrowheads indicate Ki67+ HF-SCs (*n* = 30 HFs each from three pairs of mice). Scale bar, 20 μm. **d,e**, Premature hair loss and graying in dKO mice by 5 mo of age (**d**) and 16 mo of age (**e**) (*n* ≥ 5 pairs of mice for each time point). **f**, KRT5 and Ki67 staining in control (telogen, telo) and dKO (telogen and anagen (ana)) HFs in 16-mo-old mice (*n* = 30 HFs each from three pairs of mice). White arrowheads indicate Ki67+ HF-SCs. White dashed lines indicate the bulge region. Red lines indicate dermal papillae. Scale bar, 20 μm. **g**, Two-photon intravital imaging of HFs in control and dKO mice (8 mo); white arrowheads denote miniaturized HFs, and red arrowheads mark escaping epithelial cells (*n* > 5 pairs of mice). Scale bar, 70 μm. **h**, Box plot of the size of the HF bulge region (mean ± s.d. = 10,423.62 ± 2,514.43 (young), 7,736.71 ± 2,913.99 (old), 3,705.76 ± 2,420.97 (dKO); *n* = 205 HFs, five young mice; *n* = 327 HFs, three old mice; *n* = 153 HFs, five dKO mice). **i**, Box plot of the percentage of HFs containing escaped epithelial cells (mean ± s.d. = 0.25 ± 1.3 (young), 5.6 ± 8.9 (old), 12.57 ± 17.20 (dKO); *n* = 205 HFs, five young mice; *n* = 327 HFs, three old mice; *n* = 153 HFs, five dKO mice). Boxes span the first to the third quartile, with the line inside the box representing the median value. Whiskers show minimum and maximum values or values up to 1.5 times the interquartile range below or above the first or third quartile if outliers are present. Data are plotted as individual points and considered outliers beyond whiskers. **j**, Longitudinal tracking of the same HFs in dKO mice. Red arrowhead points to the same miniaturizing HF. The red dashed line in the image from day 3 marks escaping epithelial cells near the HF-SC compartment. Only three cells are left in the HF at day 26. Scale bar, 70 μm. Data in **b,c,f,h,i** were assessed with two-sided *t*-tests.

of SOX9, a master TF governing the HF-SC fate[43–45] (Fig. 5h). In addition, dKO HFs continued to grow and cycle when they retained HF-SCs within the bulge (Extended Data Fig. 5i). In sum, these analyses reveal that HF-SCs, in the absence of *Foxc1* and *Nfatc1*, have severely compromised cell adhesion and ECM gene expression, which resembles the downregulation of these genes during aging.
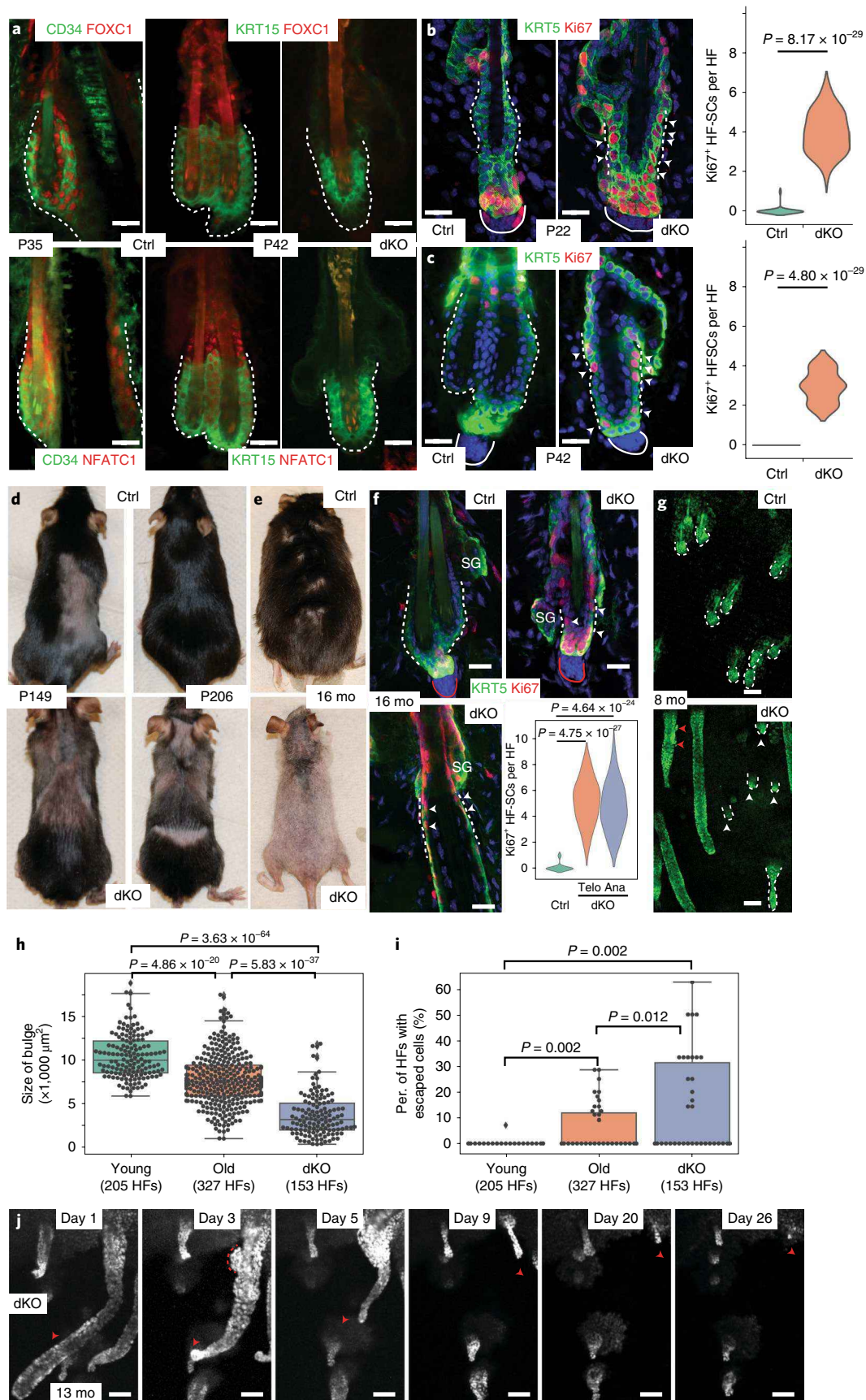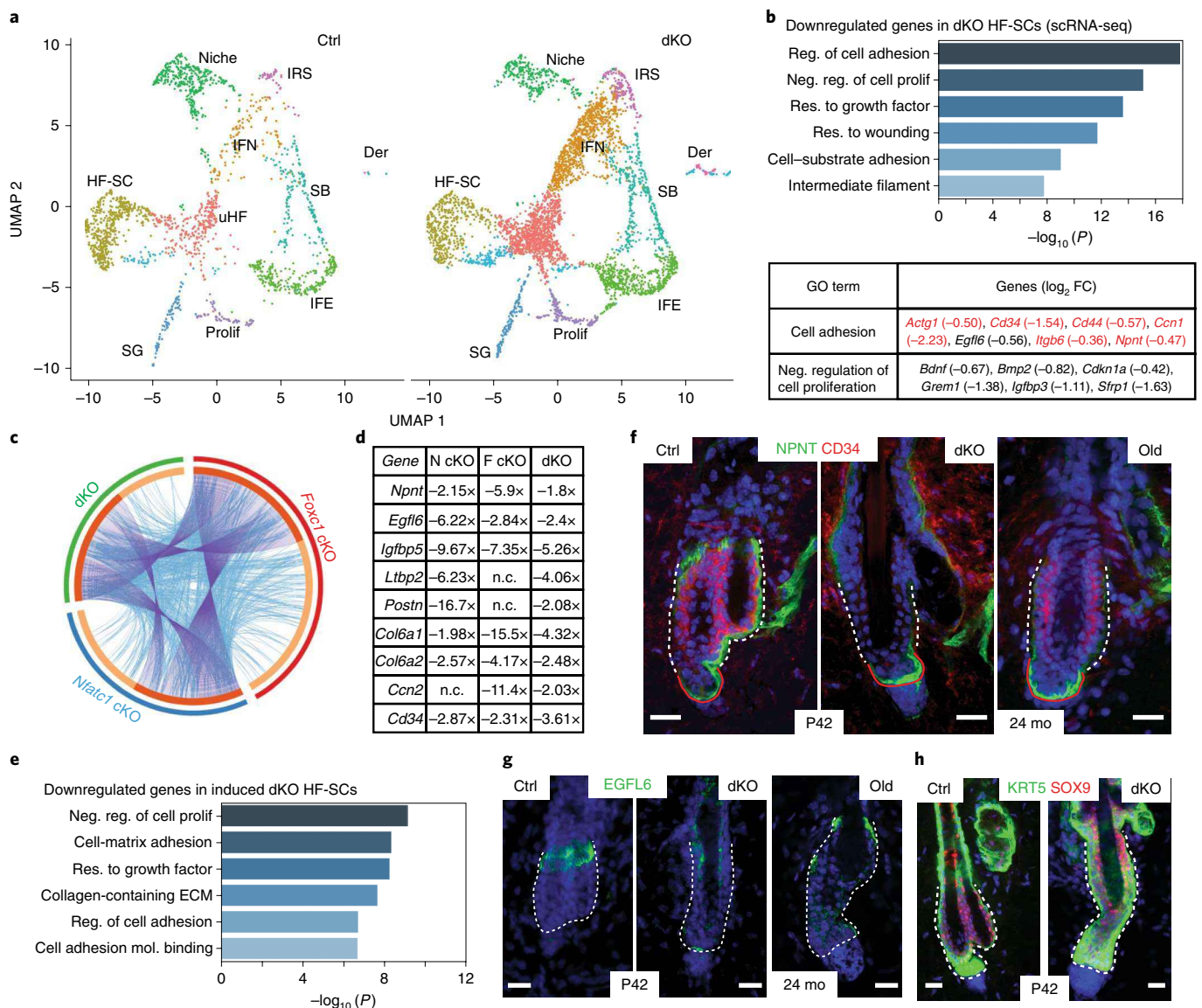
Fig. 5 | Transcriptomic analysis of dKO HF-SCs. a, UMAP clustering of control (left) and dKO (right) mouse skin samples. Major cell types are characterized using marker genes and color coded with cell identity. Der, dermal. **b**, Highly enriched GO terms in downregulated genes and selected differentially expressed genes in dKO HF-SCs. Red-colored genes are also downregulated in old HF-SCs. **c**, A Circos plot of downregulated genes in *Nfatc1*-cKO, *Foxc1*-cKO and induced dKO HF-SCs. Purple curves link identical genes, colored in dark orange, among all three datasets; blue curves link genes that belong to the same enriched GO term among the datasets. Unique genes from each dataset are colored in light orange. **d**, HF-SC-enriched cell adhesion and ECM genes and their expression change in each cKO and induced dKO strain. **e**, Highly enriched GO terms in downregulated genes in *Krt15-CrePR*-mediated dKO HF-SCs. Mol., molecule. **f,g**, NPNT, CD34 and EGFL6 IF signals in the HF-SC compartment in the second telogen (P42) and in old mice (representative images are from three pairs of mice). **h**, SOX9 IF signals in control and dKO HFs. Dashed lines mark the HF-SC compartment. Scale bar, 20 µm in **f**–**h**.

Enhancer–promoter loops mediated by FOXC1 and NFATC1. To investigate how *Foxc1* and *Nfatc1* regulate HF-SC-specific cell adhesion and ECM gene expression, we next performed single-cell ATAC-seq (scATAC-seq) on control and dKO animals at P28. We detected a median of 19,512 fragments per cell in controls and 17,392 fragments per cell in dKO mice. We clustered total epithelial cells using a t-distributed stochastic neighbor embedding (*t*-SNE) technique based on open-chromatin signatures determined by ATAC-seq[46,47] (Extended Data Fig. 8a). To validate whether scATAC-seq can correctly distinguish IFE and HF-SC lineages, we generated total open-chromatin landscapes of control IFE cells and HF-SCs and compared them with bulk ATAC-seq datasets generated from flow cytometry-purified IFE[48] and HF-SC populations.

Indeed, open-chromatin profiles of IFE and HF-SC populations detected in scATAC-seq and bulk ATAC-seq data matched closely (Fig. 6a). We next examined enriched TF motifs in IFE- and HF-SC-specific open-chromatin regions. We found that GATA3–GATA6, GRHL2–GRHL3, p63 and KLF motifs were highly enriched in IFE-specific regions, and LHX2, SOX9 and FOXC1 motifs were highly enriched in HF-SC-specific regions (Fig. 6b), consistent with previous studies documenting functions of these TFs in these epithelial lineages[7,10,45,49–53].

Next, we examined how the loss of *Foxc1* and *Nfatc1* affected open-chromatin landscape by using aggregated scATAC-seq data. In support of the notion that *Foxc1* and *Nfatc1* are specific to the HF but are not expressed in IFE cells, cellular states determined by

open-chromatin signatures revealed largely overlapping and similar populations of control and dKO IFE cells. Notably, cellular states of HF-SCs determined by open-chromatin signatures were different between control and dKO mice (Fig. 6c), in contrast to our scRNA-seq results (Fig. 5a). These data indicate that scATAC-seq is more sensitive to cellular state changes than scRNA-seq, likely due to the much higher number of uniquely identified open-chromatin regions as compared to the number of genes detected in single cells. Indeed, we identified 3,980 open-chromatin regions that were significantly reduced in dKO HF-SCs (Extended Data Fig. 8b). When we searched for enrichment of TF motifs in these regions, we identified FOXC1 and NFATC1 motifs as the top two most highly enriched TFs (Extended Data Fig. 8c). Interestingly, we also found that the KLF4 motif was the third most highly enriched motif.

We next examined how FOXC1 and NFATC1 coregulate HF-SC-enriched cell adhesion and ECM genes. CD34 is one of the most specific markers for HF-SCs[40–42], and its expression was reduced in aged HF-SCs[8], in each of *Foxc1*- and *Nfatc1*-single cKO strains, and completely abolished in dKO mice (Fig. 5f and Extended Data Fig. 7d–f). Multiple FOXC1- and NFATC1-motif-containing open-chromatin regions were identified at the *Cd34* locus (Fig. 6d). Interestingly, the transcription start site (TSS) and several enhancers of *Cd34* were uniquely open in HF-SCs but not in IFE cells, mirroring the gene expression pattern in these two lineages. In dKO mice, a FOXC1-motif-containing site lost open-chromatin signals, and the TSS and an NFATC1-motif-containing site also showed strongly reduced open-chromatin signatures (Fig. 6d). Given the complete loss of CD34 expression in dKO mice, these data suggest that the open state of these FOXC1- and NFATC1-dependent enhancers is required for *Cd34* expression in HF-SCs. Similarly, *Actg1*, *Npnt*, *Col6a1* and *Col6a2* loci also contain FOXC1- and NFATC1-dependent, HF-SC-specific open-chromatin regions (Extended Data Fig. 8d–f). Notably, *Actg1* is widely expressed in both IFE cells and HF-SCs (Extended Data Fig. 3g). However, a FOXC1-motif-containing open-chromatin region was robustly detected in control HF-SCs but not in dKO HF-SCs or IFE samples (Extended Data Fig. 8d). In support of the regulation of *Actg1* by FOXC1, *Actg1* was downregulated in old, *Foxc1*-cKO and dKO HF-SCs but not in *Nfatc1*-cKO HF-SCs or in old IFE cells. These data highlight HF-SC-specific regulation for a widely expressed cell adhesion gene.

Recent studies demonstrate that scATAC-seq can provide insights into enhancer–promoter interactions by computing the co-accessibility of open-chromatin regions in single cells[46,54]. We next examined the effect of FOXC1 and NFATC1 on local genome organization and enhancer–promoter interactions by computing Cicero co-accessibility[54]. Because cell adhesion and ECM genes such as *Actg1*, *Cd34*, *Col6a1*, *Itgb6* and *Npnt* and signaling genes such as *Bmp2* and *Fgf18* harbored FOXC1- and NFATC1-motif-containing enhancers and were strongly downregulated in dKO and aged HF-SCs, we examined enhancer–promoter interactions in their genomic loci. Enhancer–promoter interactions were generally sparse or absent for these genes in IFE cells, consistent with their HF-SC-specific expression. By contrast, many strong interactions were detected for these genes in control HF-SCs (Fig. 6e,f

and Extended Data Fig. 9). The majority of these HF-SC-specific interactions, however, were compromised, and aggregated Cicero co-accessibility scores were reduced in dKO HF-SCs, correlating with their reduced gene expression. As a control, aggregated Cicero scores remained unchanged for *Krt14*, a highly expressed gene that is not affected by dKO of *Nfatc1* and *Foxc1* (Extended Data Fig. 9c). However, the score was different for *Krt14* in IFE cells and HF-SCs, perhaps reflecting different transcriptional controls of *Krt14* in these cell lineages. To determine TFs underlying reduced enhancer–promoter interactions in dKO mice, we searched open-chromatin regions with reduced Cicero scores. The KLF4 motif was the most highly enriched, followed by NFATC1 and FOXC1 motifs (Fig. 6g). These data reveal that FOXC1 and NFATC1 control cell adhesion, ECM and signaling genes by promoting enhancer–promoter interactions specifically in HF-SCs.

Disintegration of the HF-SC compartment in *Foxc1*;*Nfatc1* dKO mice. To visualize cellular activities underlying HF miniaturization and hair loss, we next examined HF-SCs using time-lapse imaging in dKO animals. In control skin, HFs mostly rested in the telogen phase, and HF-SCs were usually quiescent with minimum cellular activities within the imaging window of 4–6 h (Fig. 7a and Supplementary Video 3). Less frequently did we observe growing HFs in the anagen phase. In these HFs, we observed limited cell migration, mostly downward movement in the outer root sheath (ORS) compartment and upward movement in the inner root sheath (IRS) (Supplementary Video 4). HF-SCs were mostly immobile, and we occasionally observed HF-SC migration, but generally no cell division was observed within the window of 4–6 h (Fig. 7b and Supplementary Video 4). In dKO skin, however, we routinely found numerous growing HFs. ORS progenitors in dKO mice rapidly migrated, mostly moving along the outer surface of HFs laterally or downward (Supplementary Video 5). We also observed strong activities of cells migrating away from the HF-SC compartment. In a 4-h imaging session, we observed an HF-SC that detached from neighboring cells and crawled along the HF. In the same HF, two HF-SCs escaped from the bulge region to the dermis. Strikingly, we observed that these two cells simultaneously changed the shape of their nuclei (24–108-min images in Fig. 7c) and squeezed through (likely) a small orifice on the BM before migrating away separately (Fig. 7c and Supplementary Video 6). Most notably, one of these two escaping cells 'jumped' more than 16 μm away from the HF in less than 30 min after the initial escape, further ruling out the possibility that it remained within the HF (Fig. 7c). These data documented the rapid escape of individual epithelial cells from the HF-SC compartment to the dermis, likely as a result of compromised cell adhesion and defective BM. In support of this, we detected individual dKO HF-SCs with strongly reduced β4 integrin signals by IF staining (Fig. 7d). These time-lapse movies thus provided direct evidence that dKO HF-SCs are a source of H2BGFP+ epithelial cells that have escaped from dKO HFs (Figs. 4g,j and 7c). Although it appeared to be random when an HF lost cells from the SC compartment into the dermis, their occurrence was generally associated with subsequent HF miniaturization and hair loss as documented in Fig. 4j.

Fig. 6 | Single-cell open-chromatin analysis of HF-SCs reveals the role of FOXC1 and NFATC1. a, *k*-means clustering comparison of open-chromatin landscapes of purified bulk IFE cells (IFE1, IFE2), aggregated single-cell IFE cells (scIFE), purified bulk HF-SCs (HF-SC1, HF-SC2) and aggregated single-cell HF-SCs (scHF-SC). **b**, Top enriched TF motifs in clusters 7–10 as classified in **a**. N.E., not enriched. **c**, *t*-SNE projection of control (light brown) and dKO (blue) epithelial cell lineages based on scATAC-seq data. Circled populations are validated as in a and cell lineage-specific open-chromatin regions. **d**, Aggregated (aggre.) scATAC-seq tracks of the *Cd34* locus annotated with FOXC1 and NFATC1 motifs. Locations of FOXC1 (green marks) and NFATC1 (red marks) motifs are indicated. Arrows point to HF-SC-specific open-chromatin regions that are lost in dKO mice, and the dashed rectangle marks the TSS of *Cd34*. **e,f**, Enhancer–promoter interactions of *Cd34* (**e**) and *Npnt* (**f**) are illustrated in control IFE cells, control HF-SCs and dKO HF-SCs. The aggregated Cicero score is calculated by summing Cicero scores of all enhancer–promoter interactions to the TSS region of each gene. Vertical lines mark the TSS, and the dashed line indicates the Cicero-score cutoff (0.2) used for calculation. **g**, Top enriched TF motifs in open-chromatin regions that have reduced Cicero scores in dKO mice, compared to controls.

To monitor the degeneration of the HF-SC compartment, we visualized miniaturized HFs before complete HF loss. Although cell migration and division were relatively infrequent, we still observed cell-division activities in these miniaturized HFs. In a miniaturized HF, we simultaneously observed a cell-division event, three nearby cells disintegrating and being released into the dermis and
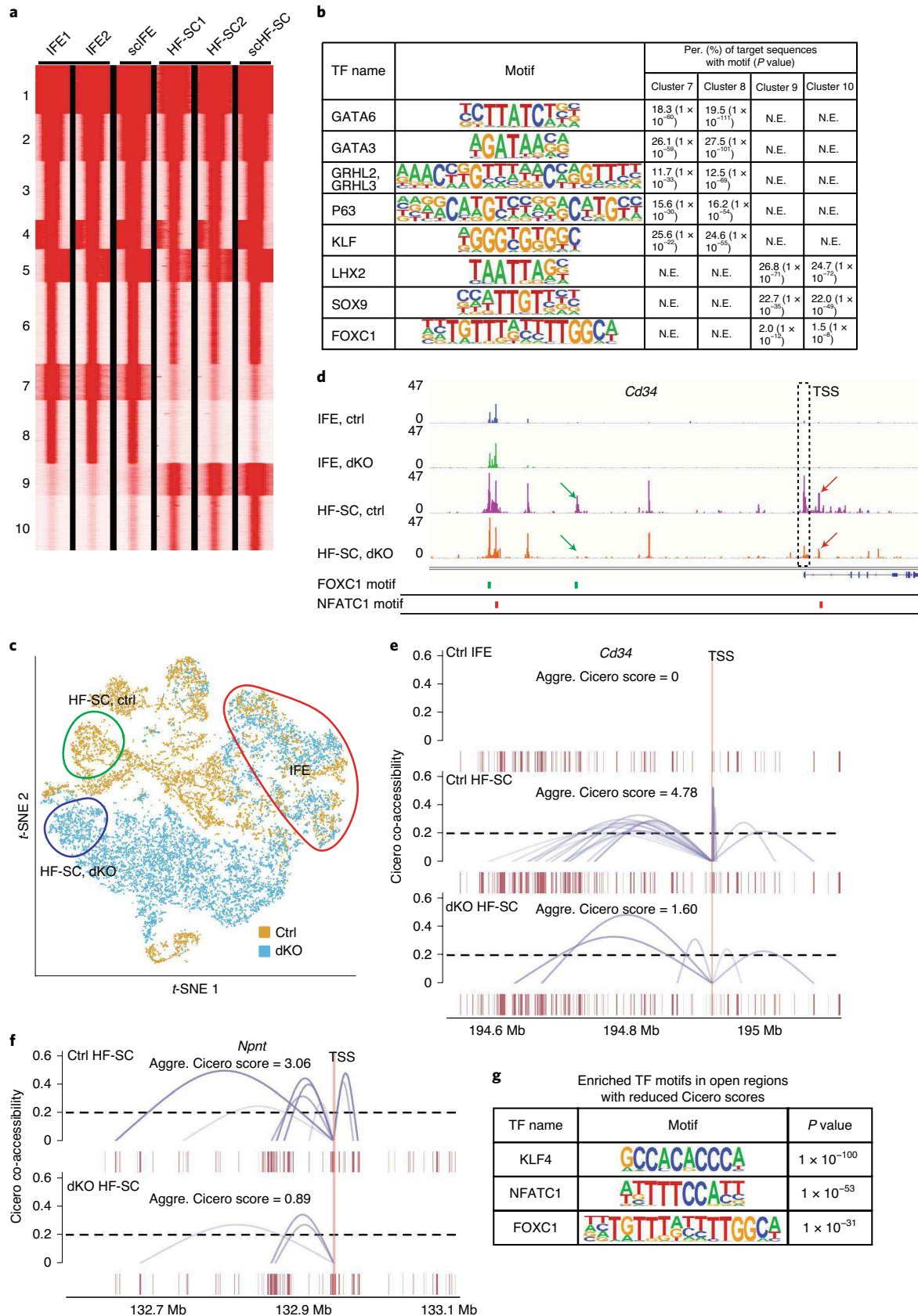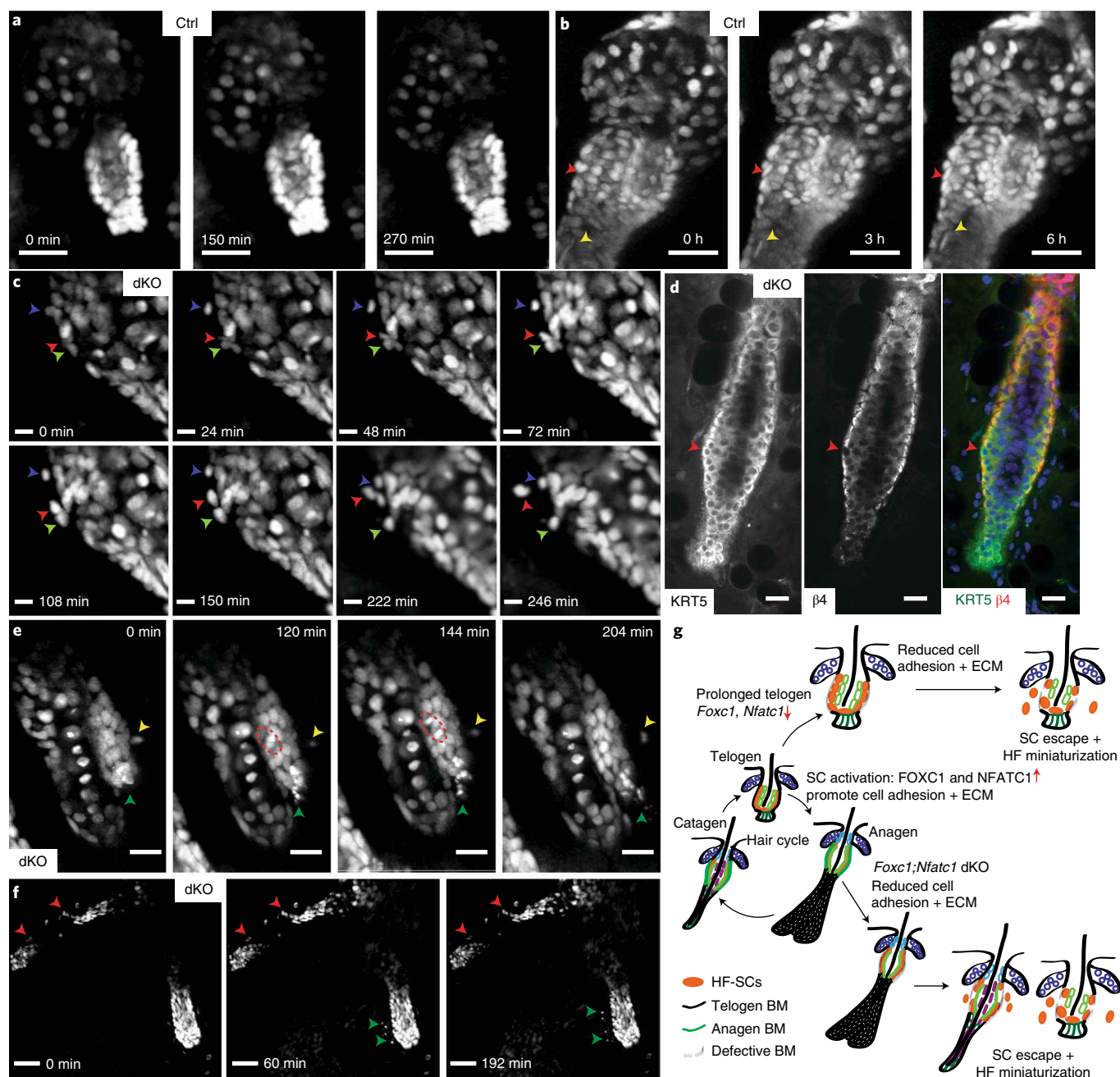
Fig. 7 | Time-lapse imaging captures HF-SCs escaping from the niche in live animals. a, Images from a 5-h movie of telogen HFs in a control reveal no cell division and migration in the HF-SC compartment. Scale bar, 30 μm. **b**, Images from a 6-h movie of anagen HFs in a control detect migrating HF-SCs and IRS cells. Red arrowheads indicate a downward-migrating HF-SC, and yellow arrowheads indicate an upward-migrating IRS cell. Scale bar, 30 μm. **c**, Images from a 4-h movie of catagen HFs in dKO mice detect HF-SCs escaping from the bulge. Blue arrowheads indicate an HF-SC detaching from the bulge; red and green arrowheads indicate two HF-SCs squeezing through the BM and escaping from the bulge region. Note the changed shape of nuclei during escape. Scale bar, 10 μm. **d**, β4 integrin IF signals in dKO HFs. Arrowheads point to disrupted BM with loss of integrin staining. Scale bar, 20 μm. **e**, Images from a 3.5-h movie of a miniaturized HF in dKO mice reveal disintegration of HF-SCs, a cell-division event and an escaped cell migrating in the dermis. Green arrowheads indicate two disintegrating cells in the miniaturized HF; red dashed circles indicate a dividing cell; and yellow arrowheads indicate a migrating cell in the dermis. Scale bar, 20 μm. **f**, Images from a 3.2-h movie of a dying HF and a miniaturizing HF in dKO mice. Red arrowheads point to escaped epithelial cells with minimum activities in the dermis. Green arrowheads point to rapidly escaping cells from a miniaturizing HF. Scale bar, 50 μm. **g**, A model illustrates HF-SC escape and HF miniaturization during aging and in the dKO HF-SC compartment.

one escaped cell migrating in the dermis within the span of 2.5 h (Fig. 7e and Supplementary Video 7). In another miniaturized HF that contained less than 20 cells, one epithelial cell moved downward and was poised to escape from the HF (Supplementary Video 8). These data suggest that miniaturized HFs are still capable of cell division but continue to lose epithelial cells due to cell escape.

Although we were unable to image the fate of these escaped cells due to limitations of the imaging protocol in live animals, they usually scattered around dying HFs, while other HFs continued to shed epithelial cells (Fig. 7f and Supplementary Video 9). These cellular activities recapitulated escaped HF-SCs observed from aged HFs (Fig. 1a,b,f,g), indicating that cell escape is a common mechanism.

To test whether the loss of individual cell adhesion and ECM genes may recapitulate cell escape and premature aging, we genetically deleted *Itgb6*, which is commonly downregulated in both aged and dKO HF-SCs and controlled by FOXC1 and NFATC1. Although genetic deletion of *Itgb6* was reported to result in juvenile baldness[55], *Itgb6*-KO animals largely recovered their normal hair coat as adults (Extended Data Fig. 10a). By 9 months, *Itgb6*-KO animals did not show any defects in hair growth or in the bulge (Extended Data Fig. 10b). Similarly, *Cd34* and *Npnt* have also been individually deleted without affecting the maintenance of HF-SCs or resulting in premature aging phenotypes[28,56]. Thus, we concluded that genetic deletion of individual cell adhesion and ECM genes may not be sufficient to recapitulate HF aging.

Collectively, our data provide evidence for a new model of SC exhaustion and HF miniaturization: dKO and aged HF-SCs fail to maintain expression of many HF-SC-specific cell adhesion and ECM genes, at least in part as a result of reduced *Foxc1* and *Nfatc1* expression. In turn, the compromised niche and reduced cell adhesion allow epithelial cells to escape from the HF-SC compartment into the dermis, resulting in SC exhaustion and eventual degeneration of HFs (Fig. 7g).

Discussion

SC escape as a mechanism of cell loss and aging. In this study, we imaged HF-SC activities during aging and in a *Foxc1;Nfatc1* dKO model in live animals. Leveraging the ability to noninvasively monitor the HF-SC compartment at a time scale ranging from hours to weeks, we observed a hitherto unreported activity of epithelial cells escaping to the dermis. Although many of these escaping cells in both aging and dKO mice are from the bulge region, it is possible that not all escaped cells are SCs. During aging, the process of cell escape is relatively slow, and we could only monitor cellular activities of single HFs at the resolution of days. We documented the disintegration of HFs accompanied by shedding epithelial cells to the dermis (Fig. 1f,g). In dKO mice, cell adhesion and ECM gene expression was strongly compromised, and this was correlated with more rapid epithelial cell escape and accelerated HF miniaturization. We captured the process of HF-SCs migrating away from the epithelial niche and into the dermis in the time span of a few hours (Supplementary Videos 6–9). Although we were unable to label the BM, the most parsimonious explanation for the profound changes of nuclear shape and the distance that these escaping cells traveled during escape (Supplementary Video 6) is that these epithelial cells squeeze through a small orifice in the defective BM and migrate into the dermis. These striking results provide direct evidence that live epithelial cells transverse the BM and reach the dermis. These unexpected observations raise a number of questions for future investigation such as how these epithelial cells remodel cell adhesion and detach from each other, gain motility and change their shape during escape.

We were unable to identify a single-cell adhesion or ECM gene, the loss of which recapitulates cell escape or the premature aging phenotype. This is perhaps not surprising because aging and tissue deterioration are generally caused by functional decline of many rather than singular contributing factors[1,2]. Indeed, the altered HF-SC microenvironment was also shown to drive HF aging[6]. Thus, HF aging is likely controlled by many different regulators. Interestingly, deletion of E-cadherin in the HF-SC compartment causes HF-SC proliferation without triggering HF-SC depletion or premature aging[57]. Furthermore, increased HF-SC proliferation is caused by loss of E-cadherin in the inner-bulge niche layer but not by the defects on the BM of the outer bulge[7,57]. Thus, the mechanism underlying cell escape and subsequent SC depletion is distinct from the defective adherens junction. Finally, this new mechanism mediated by epithelial cell escape likely functions in parallel with well-studied cell-exhaustion mechanisms such as cell death and senescence and adds a new layer of biology to tissue degeneration.

Homeless epithelial cells in aged skin. Using live imaging, we uncovered the presence of escaped, homeless epithelial cells in the dermis of aged and dKO skin. Judging by their *Krt14*-H2BGFP transgene label and their rapid escape through the BM, it is likely that these cells do not undergo profound cell fate changes such as epithelial-to-mesenchymal transition before their escape. These epithelial cells also persist in the dermis rather than immediately initiating programmed cell death such as anoikis upon escape (Fig. 1f,g and Supplementary Video 9). These observations raise important questions such as whether these escaped cells can self-renew or divide in the dermis, how they interact with the foreign environment including dermal fibroblast cells, adipocytes and immune cells and whether these escaped cells play any role in tumorigenesis during aging. These questions warrant future investigation of the fate of escaped cells in normal and pathological conditions.

Mechanisms governing SC quiescence and the niche. Our data suggest that HF-SC quiescence and their niche integrity are coupled through the function of FOXC1 and NFATC1. Our previous study suggests that HF-SC activation promotes the expression of *Foxc1*, and, in turn, FOXC1 reinforces quiescence by inducing *Nfatc1* and *Bmp2/6* expression in activated HF-SCs[10]. Furthermore, *Foxc1*-mediated HF-SC depletion has been linked to defective adherens junctions, although deletion of E-cadherin does not cause HF-SC depletion or premature aging[7,57]. Now, by examining transcriptomes that are controlled by *Foxc1* and *Nfatc1*, we find that these two TFs coregulate a large number of HF-SC-specific cell adhesion and ECM genes, including *Cd34*, *Npnt* and *Itgb6*. Importantly, we show that the lack of HF-SC division in prolonged telogen during aging also reduces *Foxc1* expression and, to a lesser extent, *Nfatc1* expression. Thus, HF-SC division may serve as a mechanism to rejuvenate cell adhesion of HF-SCs through the upregulation of *Foxc1*.

Our study has further revealed that the loss of SC quiescence per se does not directly cause SC exhaustion. Indeed, increased HF-SC proliferation does not deplete HF-SCs[57]. Furthermore, we observed numerous rapidly growing HFs when macroscopic hair loss was already widespread (Fig. 4g). Instead, dKO HF-SCs downregulated cell adhesion and ECM genes and escaped from the defective niche, resulting in excessive cell loss and hair degeneration. In support of this view, we still observed cell-division and escape events concurrently in miniaturized HFs (Supplementary Video 7). This model of SC exhaustion provides a new framework for studying SC quiescence and integrity of the SC niche.

Methods

Mice. All experiments were carried out following IACUC-approved protocols and guidelines at CU Boulder and Northwestern, respectively. Mice were bred and housed according to guidelines of the IACUC at a pathogen-free facility at the University of Colorado at Boulder and at Northwestern University Feinberg School of Medicine. The following mouse lines were used: *K14-Cre* (E. Fuchs, Rockefeller University), *K14*-H2BGFP (E. Fuchs, Rockefeller University), *Foxc1*^fl/fl^, *Foxc1*-LacZ, *Nfatc1*^fl/fl^, *Itgb6*^−/−^ (D. Sheppard, University of California, San Francisco), *K15-CrePR* (Jackson Laboratory, 005249) and *Rosa26*-LSL-tdTomato (Jackson Laboratory, 021876).

K15-CrePR induction was performed by topical application of 4% RU486 (dissolved in ethanol) from P22 to P28 for 7 consecutive days. Samples were collected 2 or 3 d later, at P30 or P31. Sex- and age-matched mice were used for flow cytometry and histology. For quantification, at least 30 HFs from at least three pairs of animals were counted. Male and female mice showed similar phenotypes, and final results were reported by combining all data.

Horizontal whole-mount staining. Back skins were embedded in optimum cutting temperature (OCT, Tissue-Tek) compound. Sections (100 μm) were prepared and incubated in PBS to remove the OCT compound. Horizontal whole-mount staining was performed as previously described[58] with minor modifications. Briefly, sections were fixed in 4% PFA for 10 min at room temperature, blocked with a mixture of 0.5% Triton X-100, 0.25% fish skin gelatin and 0.5% skim milk powder in PBS (blocking solution) for 1 h at room temperature and incubated overnight with primary antibodies at 4 °C. Antibodies were diluted in blocking solution. After incubation, sections were washed three times with 1× PBS for

2–3 h. Secondary antibodies were added at a dilution of 1:1,000 together with 5 µg ml^{-1} Hoechst 33342 (Invitrogen) for 1 h at room temperature, followed by washing three times with 1× PBS for 30 min. Sections were then placed on slides in VECTASHIELD antifade mounting medium (Vector Laboratories, H-1000) under a dissection microscope to ensure correct orientation and then covered with coverslips for imaging. Confocal imaging of whole-mount staining was performed on a Nikon A1 laser scanning confocal microscope with either a 20×, 0.75-numerical aperture (NA) or a 100×;, 1.49-NA objective lens, and images were acquired with NLS Elements (Nikon) software in the Light Microscopy Core Facility of the University of Colorado, Boulder.

Cryosectioning and immunostaining. OCT-embedded tissues were sectioned to 20–30 µm and fixed with 4% PFA for 10 min at room temperature. Sections were permeabilized for 10 min at room temperature with 0.1% Triton X-100 in 1× PBS. When staining with mouse monoclonal antibodies, we used the mouse-on-mouse basic kit (BMK-2202, Vector Laboratories). Otherwise, blocking was performed with 5% normal serum of the same species that the secondary antibody was raised in. Sections were incubated with primary antibody overnight at 4 °C. After incubation with primary antibodies, sections were washed three times in 1× PBS and incubated for 1 h at room temperature with Alexa Fluor 594–, Alexa Fluor 488- or Alexa Fluor 647-conjugated secondary antibodies (1:2,000, Invitrogen–Molecular Probes). Nuclei were stained with Hoechst 33342 (1:5,000, Invitrogen).

Flow cytometry cell sorting. Sex- and hair cycle-matched mice were euthanized and collected for dissection. We first shaved the hair coat and applied nair hair removal lotion (Amazon, 22339) for around 3 min. After wiping off the lotion and washing away leftover hair shafts, back skin was dissected, and subcutaneous fat was removed using a blade. A small part of the skin sample was embedded in OCT, and the remaining skin sample was minced and incubated with 0.25% collagenase (Worthington, LS004188) in 4–6 ml 1× HBSS buffer at 37 °C for 2 h with rotation. A 5-ml serological pipet was used to further separate the epidermis from the dermis at the 1-h incubation time. After collagen treatment, we added 10 ml cold PBS and centrifuged the sample at 400*g* for 10 min at 4 °C. The pellet was resuspended with prewarmed 0.25% trypsin–EDTA (Gibco) for 8 min at 37 °C, and the digestion was immediately blocked by adding 10 ml cold 1× PBS with 3% chelated FBS. The suspension was extensively triturated with a 10-ml pipette and passed over a 40-µm cell strainer, followed by centrifugation at 400*g* for 5 min at 4 °C. Pelleted cells were resuspended in cold 1× PBS with 3% chelated FBS. Cells were incubated with appropriate antibodies for 1 h on ice. DAPI was used to exclude dead cells. HF-SCs from *K14-Cre*-based experiments were isolated by enriching for DAPI$^-$K14-H2BGFP^{hi}SCA1^{lo}α6^{hi}CD34^{hi} cells. HF-SCs from *K15-CrePR*-based experiments were isolated by enriching for DAPI$^-$K14-H2BGFP^{hi}tdTomato^{hi}SCA1^{lo}CD34^{hi} cells. The following antibodies were used: anti-integrin α6 (CD49f, 1:75; eBioscience, PE conjugated, 12-0495; APC conjugated, 17-0495), anti-CD34 (1:50; eBioscience, eFluor 660 conjugated, 50-0341), anti-SCA1 (Ly-6A/E, 1:500; eBioscience, PerCP-Cy5.5 conjugated, 45-5981). Flow cytometry was performed on the MoFlo XDP machine (Beckman Coulter). Flow cytometry data were analyzed with FlowJo.

RNA-seq assay. Total RNA from flow cytometry-purified cells was isolated using TRIzol (Invitrogen), and RNA quality was assessed with the Agilent 2100 bioanalyzer. RNA with integrity numbers >8 was used to perform RNA-seq assays. Libraries were prepared following the manufacturer's protocol (NEBNext Ultra Directional RNA Library Prep kit). cDNA libraries were checked for quality with the bioanalyzer before being sent out for sequencing to the Genomics and Microarray Core Facility at the University of Colorado Denver on the Illumina NovaSeq 6000.

Omni-ATAC-seq assay. ATAC-seq was performed as previously described[59] with the following modifications: an average of 50,000 flow cytometry-sorted HF-SCs were collected in PBS containing 3% chelated FBS and pelleted by centrifugation for 5 min at 500*g* and 4 °C. Cell pellets were resuspended in 50 µl lysis buffer containing 10 mM Tris-HCl, pH 7.4, 10 mM NaCl, 3 mM MgCl$_2$, 0.1% Igepal CA-630, 0.1% Tween-20 and 0.01% digitonin and incubated on ice for 3 min. After the incubation, we added 1 ml wash buffer containing 10 mM Tris-HCl, pH 7.4, 10 mM NaCl, 3 mM MgCl$_2$ and 0.1% Tween-20 and inverted the tube three times to mix. Nuclei were then pelleted by centrifugation for 15 min at 500*g* and 4 °C. The supernatant was carefully discarded, and nuclei were resuspended in 50 µl reaction buffer containing 5 µl Tn5 transposase and 25 µl TD buffer (Nextera DNA Sample Preparation kit, Illumina), 16.5 µl PBS, 0.5 µl 1% digitonin, 0.5 µl 10% Tween-20 and 5 µl H$_2$O. The reaction was incubated at 37 °C for 30 min with rotation, terminated by adding 10 µl clean-up buffer (900 mM NaCl, 300 mM EDTA) and immediately purified using the MinElute PCR Purification kit (Qiagen). After purification, DNA samples were quantified using a NanoDrop, and 50 ng DNA was used for library construction. Library amplification was performed for 13 cycles following the manufacturer's protocol (Nextera DNA Sample Preparation kit, Illumina) except that we used 2.5 µl of each primer and a 2-min extension time in the PCR reaction. Libraries were size selected to enrich for inserts of150–1,000 bp in size, checked for quality with the bioanalyzer and paired-end sequenced for at least 40 million reads per sample.

Single-cell ATAC-seq assay. Cells from both wild-type and dKO animals were collected from a flow cytometry-sorting machine with cell surface proteins and H2BGFP signals such that epidermal cells and HF cells were at a 1:3 ratio. In total, 10,000 cells were used for preparation of both WT and dKO samples for scATAC-seq. Libraries were prepared using the 10x Chromium Single Cell ATAC Library & Gel Bead kit (PN-1000110). In brief, cell nuclei were isolated, and nuclear suspensions were incubated in a transposition mix to fragment DNA and add adaptor sequence to the end of DNA fragments. Single-nucleus resolution was achieved using 10x barcoded gel beads, partitioning oil and a master mix on a Chromium Chip E. Libraries were constructed using a 10x sample index plate and double size selected from 150 bp to 1,000 bp.

Intravital live imaging. Intravital live imaging was performed as previously described[23,24] with modifications. Mice used for imaging was sedated using 2% oxygen and ~1–2% isoflurane. Once the mouse was fully sedated (~5 min), it was put on a warm pad at 37 °C. Oxygen and isoflurane levels were maintained during the course of imaging. Night-time ointment (Genteal, NDC 0078-0473-97) was applied to keep the eyes moisturized. A 30-gauge needle and tattoo ink were used to mark the region (it is best to mark the region at least 1 d before imaging to allow for healing). A custom-manufactured spatula was used to stretch and flatten the region of interest (near the tattoo ink) and was maintained at an adjustable height. Double-sided tape was used to adhere the lower side of ear onto the spatula. After applying long-lasting Genteal gel (0078-0429-47) to the region of interest, a second adjustable spatula, glued to a coverglass on one end, was gently pressed down on the ear so that the coverglass was directly on top of the region. A second round of long-lasting Genteal was applied to the coverglass (the Genteal gel should cover a region large enough for the objective to move around, and a sufficiently large amount should be used to keep the tip of objective immersed during imaging). We used the Olympus FVMPE-RS multiphoton imaging system to acquire images. The lasers we used were the InSight X3 with wavelength set to 920 nm for GFP signals and the Mai Tai HP with wavelength set to 860 nm for second-harmonic-generation signals. Emission wavelengths were 510 nm and 430 nm, respectively. We used 10× and 25× objectives for images. During the imaging session, the light should be turned off, and the stages and scope should be covered with a black curtain to avoid exposure to light. After the imaging session is complete, the mouse was kept in oxygen for around 10 min to recover before sending it back to the cage.

Two-photon image processing and quantification. Two-photon images were acquired using FluoView software from Olympus. Images were opened using Fiji (ImageJ) and converted to TIF format using 'Fiji > plugins > bio-formats > bio-formats-exporter'. Time-lapse images were aligned using 'plugins > registration > descriptor-based series registration (2d/3d +t)' before being exported. Exported TIF files were further converted to Imaris files using the Imaris File Converter. Imaris x64 9.2.1 was used to open files for further analysis. Images were adjusted on the *x*, *y* or *z* plane and smoothed with a Gaussian filter for better visualization. Movies were also adjusted and generated with Imaris. For HF quantification, 3D pictures were opened in Imaris, and then the epidermis and upper HF regions were cropped out. Next, 3D rendering was applied to leftover bulge regions to model the surface area. The surface area output was used for quantification and plotting. For HF miniaturization, we used the smallest HF in young samples as the cutoff; any HF smaller than the cutoff was counted as miniaturized. To quantify the number of HF-SCs, we used 3D two-photon images to select one sagittal plane and count all HF-SCs in the outer layer.

To quantify the HF fate, we tracked 78 HFs in total for at least 16 d and monitored HF morphological changes. We defined regeneration as HFs that are cycling with no signs of shrinkage while in telogen, degeneration as noncycling HFs undergoing miniaturization or cycling HFs becoming smaller in telogen and quiescence as noncycling HFs with no significant size change during tracking.

To quantify FOXC1 and NFATC1 immune-staining signals in HF-SCs, we co-stained with CD34 to label the bulge region and HF-SCs. Images were then converted to Imaris format for further quantification. Briefly, we used the Imaris Surface module to manually select a circle of fixed size in the nucleus of HF-SCs. The mean and/or median intensity of each channel in the selected region was obtained from the statistical tab.

RNA-seq analysis. RNA-seq reads (150 nt, paired end) were aligned to the mouse genome (NCBI37/mm10) using HISAT2 (version 2.1.0)[60]. The resulting SAM files were converted to BAM files using SAMtools (version 1.3.1)[61]. Expression of each gene was calculated from the resulting BAM alignment file by HTSeq[62]. Differentially expressed genes were determined using DESeq2 (ref. [63]) with an adjusted *P*-value cutoff of 0.05. GO analysis was performed using Metascape[64]. Selected GO terms were from Metascape results along with the gene lists.

Single-cell RNA-seq analysis. The Cell Ranger Single-Cell Software Suite was used to perform barcode processing and single-cell 3′ gene counting (http://software.10xgenomics.com/single-cell/overview/welcome). Barcodes, features and matrix files were loaded into Seurat 3.0 (ref. [26]) for downstream analysis (https://satijalab.org/seurat/vignettes.html). For each sample, the analysis pipeline followed

instructions in the guided tutorial. Cells were filtered using nFeature_RNA (>200 and <5,000) and the mitochondrial percentage (<10%). In addition, cell cycle regression was used to regress out addition variation from cell cycle genes. After clustering and UMAP dimension reduction, cluster markers were used to identify distinct cell populations. For comparison between different samples, all samples were integrated to promote identification of common cell types and enable comparative analysis[65]. All differential analyses were based on the nonparametric Wilcoxon rank-sum test. Average log (FC) values were converted to $\log_2$ (FC) values for consistency with bulk RNA-seq data. Genes with adjusted P values less than 0.05 were used for GO term analysis.

To recluster specific cell populations, we first subset the cells of interest and then re-ran the analysis pipeline with modifications for UMAP resolution.

For differential gene plots, we used both default Seurat options and SCANPY[66]. Note that we used cell cycle regression for initial clustering of total populations; but, for pseudotime analysis, we did not regress out cell cycle genes to capture differentiation information. After clustering, we were able to resolve LGR6$^+$ HF-SCs, which we thus named the upHFSC population. Next, we kept only HF lineages including HF-SCs, UpHFs, infundibular cells, niche cells, HGs, UpHFSCs and SGs based on Seurat clustering. Finally, we converted the Seurat object to a single-cell experiment for standard downstream Monocle 3 pseudotime analysis[29]. After obtaining pseudotime scores for each cell, we first filtered out all cells without scores (which are mostly SGs) and then added the information back to the Seurat object for further plotting.

ATAC-seq and motif analysis. ATAC-seq reads (paired end) were aligned to the mouse genome (NCBI37/mm10) using Bowtie 2 (version 2.2.3)[67]. Duplicate reads were removed with Picard tools (http://broadinstitute.github.io/picard/). Mitochondrial reads were removed, and peaks were called on each individual sample by MACS (version 2.0.9)[68]. Peaks from different ATAC-seq samples were merged for downstream analysis. De novo motif discovery was performed using HOMER[69]. Motif scanning was performed with MEME (5.0.3)[70]. BED files were converted to FASTA files by bedtools getfasta[71], and motifs discovered by HOMER were used to scan for instances in open-chromatin regions. HOMER motifs were also converted to MEME format with the R package from GitHub (https://gist.github.com/rtraborn/e395776b965398c54c4d). For IGV visualization[72], we first concatenated all peaks from samples of interest and converted them into a GTF file, counted the number of reads mapped in peaks and then normalized all samples using 'bedtools genomecov -scale' to obtain bedGraph files. Igvtools toTDF was used to obtain TDF files for final visualization.

Single-cell ATAC-seq analysis. FASTQ files were collected from the sequencing facility and concatenated together. We used cellranger-atac (version 3.0.1) counts with the reference downloaded from the 10x Genomics website. Loupe Cell Browser (version 3.1.0) was used to generate a t-SNE plot of wild-type and dKO samples. We used graph-based clustering for P28 control samples and k-means-based clustering for P28 dKO samples for better identification of subpopulations.

IFE and HF-SC populations were first extracted from the BAM file of the cellranger-atac output file. First, we extracted cluster IDs of each population and used suggested methods from 10x Genomics (https://kb.10xgenomics.com/hc/en-us/articles/360022448251-Is-there-way-to-filter-the-BAM-file-produced-by-10x-pipelines-with-a-list-of-barcodes-) to subset BAM files specific for each population. To predict the *cis*-regulatory landscape from scATAC-seq data, we used the R package Cicero[54] to infer enhancer and promoter interactions. The pipeline was performed according to instructions in the tutorial. Cicero connection lists were exported from R and saved for further analysis. Cicero connection lists were exported from R and saved for further analysis. For connection scores at TSSs, we first downloaded the mouse gene coordinate GFF file from the UCSC genome browser and then we extracted gene TSS sites based on gene coordinates and strand information. Cicero peaks were imported to Python, and we used pandas to covert to the BED file format. Formatted Cicero BED files were used to intersect with TSS BED files to extract peaks connected to TSS sites and corresponding connection scores. For each individual gene, connection scores were first filtered with 0.2 as the cutoff, and then all connections were summed up as the total score. For global reduced enhancer–promoter interactions, we first used all connection scores greater than and equal to 0.16 to reduce noise and then organized and formatted all peaks from control and dKO samples for comparison. We considered any interactions with greater than or equal to 0.2 as changed interactions and those with less than or equal to 0.1 as background interactions. All peaks with corresponding interactions were pooled, peaks with TSSs were filtered out, and then we used HOMER[69] for de novo motif discovery.

k-means clustering of ATAC peaks. To compare open-chromatin signals across multiple samples, k-means clustering was performed using seqMINER (version 1.3.4)[73]. BAM files were first converted to BED files using bedtools bamtobed. To normalize across samples for depth of sequencing, we downsampled each BED file to 20 million reads for input. Peaks were called by MACS2 from all bulk ATAC-seq data. Next, peaks called from bulk data were concatenated, sorted, merged and then used as genome coordinates. Signals were calculated in a 1.5-kb region (± 750 bp) surrounding the center of the peak with 50-nt bins.

Statistics and study design. In general, all sequencing experiments (RNA-seq, ATAC-seq) were repeated on at least two pairs of control and cKO or dKO samples per experiment. scATAC-seq was performed with one pair of control and dKO samples at the same time on the same chip to avoid batch effects. All experiments were designed such that there were always littermate controls. All statistical tests were performed as indicated in figure legends. No statistical methods were used to predetermine sample size. Experiments were not randomized, and investigators were not blinded to allocation during experiments or outcome assessment, except when stated.

Statistics and reproducibility. Results in Fig. 1a,b,f–i were repeated with at least three different animals. Results in Fig. 4a,j were repeated with at least three different animals. Results in Fig. 5h were repeated with at least three different animals. Results in Fig. 7a,b,d–f were repeated with at least three different animals. Results in Fig. 7c were observed in two different animals. Results in Extended Data Figs. 1a,b,d,h, 4a–c, 5b,e,g,i, 7a and 10b were repeated with at least three animals.

Reporting Summary. Further information on research design is available in the Nature Research Reporting Summary linked to this article.

Data availability

All sequencing data were deposited to NCBI–GEO SuperSeries under accession number GSE133648.

References

1. Campisi, J. et al. From discoveries in ageing research to therapeutics for healthy ageing. *Nature* **571**, 183–192 (2019).
2. López-Otín, C., Blasco, M. A., Partridge, L., Serrano, M. & Kroemer, G. The hallmarks of aging. *Cell* **153**, 1194–1217 (2013).
3. Dall'Ara, E. et al. Longitudinal imaging of the ageing mouse. *Mech. Ageing Dev.* **160**, 93–116 (2016).
4. Pittet, M. J. & Weissleder, R. Intravital imaging. *Cell* **147**, 983–991 (2011).
5. Florian, M. C. et al. A canonical to non-canonical Wnt signalling switch in haematopoietic stem-cell ageing. *Nature* **503**, 392–396 (2013).
6. Ge, Y. et al. The aging skin microenvironment dictates stem cell behavior. *Proc. Natl Acad. Sci. USA* **117**, 5339–5350 (2020).
7. Lay, K., Kume, T. & Fuchs, E. FOXC1 maintains the hair follicle stem cell niche and governs stem cell quiescence to preserve long-term tissue-regenerating potential. *Proc. Natl Acad. Sci. USA* **113**, E1506–E1515 (2016).
8. Matsumura, H. et al. Hair follicle aging is driven by transepidermal elimination of stem cells via COL17A1 proteolysis. *Science* **351**, aad4395 (2016).
9. Sinha, M. et al. Restoring systemic GDF11 levels reverses age-related dysfunction in mouse skeletal muscle. *Science* **344**, 649–652 (2014).
10. Wang, L., Siegenthaler, J. A., Dowell, R. D. & Yi, R. Foxc1 reinforces quiescence in self-renewing hair follicle stem cells. *Science* **351**, 613–617 (2016).
11. Rossi, D. J. et al. Deficiencies in DNA damage repair limit the function of haematopoietic stem cells with age. *Nature* **447**, 725–729 (2007).
12. Janzen, V. et al. Stem-cell ageing modified by the cyclin-dependent kinase inhibitor p16INK4a. *Nature* **443**, 421–426 (2006).
13. Sharpless, N. E. & DePinho, R. A. How stem cells age and why this makes us grow old. *Nat. Rev. Mol. Cell Biol.* **8**, 703–713 (2007).
14. Cheung, T. H. & Rando, T. A. Molecular regulation of stem cell quiescence. *Nat. Rev. Mol. Cell Biol.* **14**, 329–340 (2013).
15. Cho, I. J. et al. Mechanisms, hallmarks, and implications of stem cell quiescence. *Stem Cell Rep.* **12**, 1190–1200 (2019).
16. Nakamura-Ishizu, A., Takizawa, H. & Suda, T. The analysis, roles and regulation of quiescence in hematopoietic stem cells. *Development* **141**, 4656–4666 (2014).
17. Yi, R. Concise review: mechanisms of quiescent hair follicle stem cell regulation. *Stem Cells* **35**, 2323–2330 (2017).
18. Cheng, T. et al. Hematopoietic stem cell quiescence maintained by p21$^{cip1/waf1}$. *Science* **287**, 1804–1808 (2000).
19. Chakkalakal, J. V., Jones, K. M., Basson, M. A. & Brack, A. S. The aged niche disrupts muscle stem cell quiescence. *Nature* **490**, 355–360 (2012).
20. Tomasetti, C. & Vogelstein, B. Variation in cancer risk among tissues can be explained by the number of stem cell divisions. *Science* **347**, 78–81 (2015).
21. Garza, L. A. et al. Prostaglandin D2 inhibits hair growth and is elevated in bald scalp of men with androgenetic alopecia. *Sci. Transl. Med.* **4**, 126ra34 (2012).
22. Shimomura, Y. et al. APCDD1 is a novel Wnt inhibitor mutated in hereditary hypotrichosis simplex. *Nature* **464**, 1043–1047 (2010).
23. Pineda, C. M. et al. Intravital imaging of hair follicle regeneration in the mouse. *Nat. Protoc.* **10**, 1116–1130 (2015).

24. Rompolas, P. et al. Live imaging of stem cell and progeny behaviour in physiological hair-follicle regeneration. *Nature* **487**, 496–499 (2012).

25. Chen, C.-C. et al. Regenerative hair waves in aging mice and extra-follicular modulators follistatin, dkk1, and sfrp4. *J. Invest. Dermatol.* **134**, 2086–2096 (2014).

26. Stuart, T. et al. Comprehensive integration of single-cell data. *Cell* **177**, 1888–1902 (2019).

27. Salzer, M. C. et al. Identity noise and adipogenic traits characterize dermal fibroblast aging. *Cell* **175**, 1575–1590 (2018).

28. Fujiwara, H. et al. The basement membrane of hair follicle stem cells is a muscle cell niche. *Cell* **144**, 577–589 (2011).

29. Cao, J. et al. The single-cell transcriptional landscape of mammalian organogenesis. *Nature* **566**, 496–502 (2019).

30. Lee, J. et al. Runx1 and p21 synergistically limit the extent of hair follicle stem cell quiescence in vivo. *Proc. Natl Acad. Sci. USA* **110**, 4634–4639 (2013).

31. Osorio, K. M. et al. Runx1 modulates developmental, but not injury-driven, hair follicle stem cell activation. *Development* **135**, 1059–1068 (2008).

32. Horsley, V., Aliprantis, A. O., Polak, L., Glimcher, L. H. & Fuchs, E. NFATc1 balances quiescence and proliferation of skin stem cells. *Cell* **132**, 299–310 (2008).

33. Keyes, B. E. et al. Nfatc1 orchestrates aging in hair follicle stem cells. *Proc. Natl Acad. Sci. USA* **110**, E4950–E4959 (2013).

34. Lien, W.-H. et al. In vivo transcriptional governance of hair follicle stem cells by canonical Wnt regulators. *Nat. Cell Biol.* **16**, 179–190 (2014).

35. Besson, V. et al. *PW1* gene/paternally expressed gene 3 (PW1/Peg3) identifies multiple adult stem and progenitor cell populations. *Proc. Natl Acad. Sci. USA* **108**, 11470–11475 (2011).

36. Kimura-Ueki, M. et al. Hair cycle resting phase is regulated by cyclic epithelial FGF18 signaling. *J. Invest. Dermatol.* **132**, 1338–1345 (2012).

37. Plikus, M. V. et al. Cyclic dermal BMP signalling regulates stem cell activation during hair regeneration. *Nature* **451**, 340–344 (2008).

38. Hsu, Y.-C., Li, L. & Fuchs, E. Transit-amplifying cells orchestrate stem cell activity and tissue regeneration. *Cell* **157**, 935–949 (2014).

39. Zhang, Y. V., Cheong, J., Ciapurin, N., McDermitt, D. J. & Tumbar, T. Distinct self-renewal and differentiation phases in the niche of infrequently dividing hair follicle stem cells. *Cell Stem Cell* **5**, 267–278 (2009).

40. Tumbar, T. et al. Defining the epithelial stem cell niche in skin. *Science* **303**, 359–363 (2004).

41. Blanpain, C., Lowry, W. E., Geoghegan, A., Polak, L. & Fuchs, E. Self-renewal, multipotency, and the existence of two cell populations within an epithelial stem cell niche. *Cell* **118**, 635–648 (2004).

42. Morris, R. J. et al. Capturing and profiling adult hair follicle stem cells. *Nat. Biotechnol.* **22**, 411–417 (2004).

43. Adam, R. C. et al. Pioneer factors govern super-enhancer dynamics in stem cell plasticity and lineage choice. *Nature* **521**, 366–370 (2015).

44. Nowak, J. A., Polak, L., Pasolli, H. A. & Fuchs, E. Hair follicle stem cells are specified and function in early skin morphogenesis. *Cell Stem Cell* **3**, 33–43 (2008).

45. Vidal, V. P. et al. Sox9 is essential for outer root sheath differentiation and the formation of the hair stem cell compartment. *Curr. Biol.* **15**, 1340–1351 (2005).

46. Buenrostro, J. D. et al. Single-cell chromatin accessibility reveals principles of regulatory variation. *Nature* **523**, 486–490 (2015).

47. Buenrostro, J. D., Giresi, P. G., Zaba, L. C., Chang, H. Y. & Greenleaf, W. J. Transposition of native chromatin for fast and sensitive epigenomic profiling of open chromatin, DNA-binding proteins and nucleosome position. *Nat. Methods* **10**, 1213–1218 (2013).

48. Naik, S. et al. Inflammatory memory sensitizes skin epithelial stem cells to tissue damage. *Nature* **550**, 475–480 (2017).

49. Rhee, H., Polak, L. & Fuchs, E. Lhx2 maintains stem cell character in hair follicles. *Science* **312**, 1946–1949 (2006).

50. Fan, X. et al. Single cell and open chromatin analysis reveals molecular origin of epidermal cells of the skin. *Dev. Cell* **47**, 21–37 (2018).

51. Kadaja, M. et al. SOX9: a stem cell transcriptional regulator of secreted niche signaling factors. *Genes Dev.* **28**, 328–341 (2014).

52. Klein, R. H. et al. GRHL3 binding and enhancers rearrange as epidermal keratinocytes transition between functional states. *PLoS Genet.* **13**, e1006745 (2017).

53. de Guzman Strong, C. et al. Lipid defect underlies selective skin barrier impairment of an epidermal-specific deletion of *Gata-3. J. Cell Biol.* **175**, 661–670 (2006).

54. Pliner, H. A. et al. Cicero predicts *cis*-regulatory DNA interactions from single-cell chromatin accessibility data. *Mol. Cell* **71**, 858–871 (2018).

55. Huang, X. Z. et al. Inactivation of the integrin β6 subunit gene reveals a role of epithelial integrins in regulating inflammation in the lung and skin. *J. Cell Biol.* **133**, 921–928 (1996).

56. Trempus, C. S. et al. CD34 expression by hair follicle stem cells is required for skin tumor development in mice. *Cancer Res.* **67**, 4173–4181 (2007).

57. Lay, K. et al. Stem cells repurpose proliferation to contain a breach in their niche barrier. *eLife* **7**, e41661 (2018).

58. Driskell, R. R. et al. Distinct fibroblast lineages determine dermal architecture in skin development and repair. *Nature* **504**, 277–281 (2013).

59. Corces, M. R. et al. An improved ATAC-seq protocol reduces background and enables interrogation of frozen tissues. *Nat. Methods* **14**, 959–962 (2017).

60. Kim, D., Langmead, B. & Salzberg, S. L. HISAT: a fast spliced aligner with low memory requirements. *Nat. Methods* **12**, 357–360 (2015).

61. Li, H. et al. The sequence alignment/map format and SAMtools. *Bioinformatics* **25**, 2078–2079 (2009).

62. Anders, S., Pyl, P. T. & Huber, W. HTSeq—a Python framework to work with high-throughput sequencing data. *Bioinformatics* **31**, 166–169 (2015).

63. Love, M. I., Huber, W. & Anders, S. Moderated estimation of fold change and dispersion for RNA-seq data with DESeq2. *Genome Biol.* **15**, 550 (2014).

64. Zhou, Y. et al. Metascape provides a biologist-oriented resource for the analysis of systems-level datasets. *Nat. Commun.* **10**, 1523 (2019).

65. Butler, A., Hoffman, P., Smibert, P., Papalexi, E. & Satija, R. Integrating single-cell transcriptomic data across different conditions, technologies, and species. *Nat. Biotechnol.* **36**, 411–420 (2018).

66. Wolf, F. A., Angerer, P. & Theis, F. J. SCANPY: large-scale single-cell gene expression data analysis. *Genome Biol.* **19**, 15 (2018).

67. Langmead, B. & Salzberg, S. L. Fast gapped-read alignment with Bowtie 2. *Nat. Methods* **9**, 357–359 (2012).

68. Zhang, Y. et al. Model-based Analysis of ChIP-Seq (MACS). *Genome Biol.* **9**, R137 (2008).

69. Heinz, S. et al. Simple combinations of lineage-determining transcription factors prime *cis*-regulatory elements required for macrophage and B cell identities. *Mol. Cell* **38**, 576–589 (2010).

70. Bailey, T. L. et al. MEME SUITE: tools for motif discovery and searching. *Nucleic Acids Res.* **37**, W202–W208 (2009).

71. Quinlan, A. R. & Hall, I. M. BEDTools: a flexible suite of utilities for comparing genomic features. *Bioinformatics* **26**, 841–842 (2010).

72. Robinson, J. T. et al. Integrative Genomics Viewer. *Nat. Biotechnol.* **29**, 24–26 (2011).

73. Ye, T. et al. seqMINER: an integrated ChIP-seq data interpretation platform. *Nucleic Acids Res.* **39**, e35 (2011).

Acknowledgements

Author contributions

R.Y. conceived the study. C.Z., D.W. and R.Y. designed experiments. C.Z. carried out most experiments and computational analysis with assistance from D.W. for IF staining and imaging. J.W. performed two-photon imaging for some control experiments. L.W. helped to analyze scATAC-seq data. W.Q. generated the *Itgb6*-KO mouse and provided samples. T.K. generated *Foxc1* mouse models. R.D. supervised computational analysis. R.Y. and R.D. were co-mentors to C.Z. R.Y. wrote the manuscript with input from all authors.

Competing interests

The authors declare no competing interests.

Additional information

Extended data is available for this paper at https://doi.org/10.1038/s43587-021-00103-w.

Supplementary information The online version contains supplementary material available at https://doi.org/10.1038/s43587-021-00103-w.

Correspondence and requests for materials should be addressed to Rui Yi.

Peer review information *Nature Aging* thanks the anonymous reviewers for their contribution to the peer review of this work.

Reprints and permissions information is available at www.nature.com/reprints.
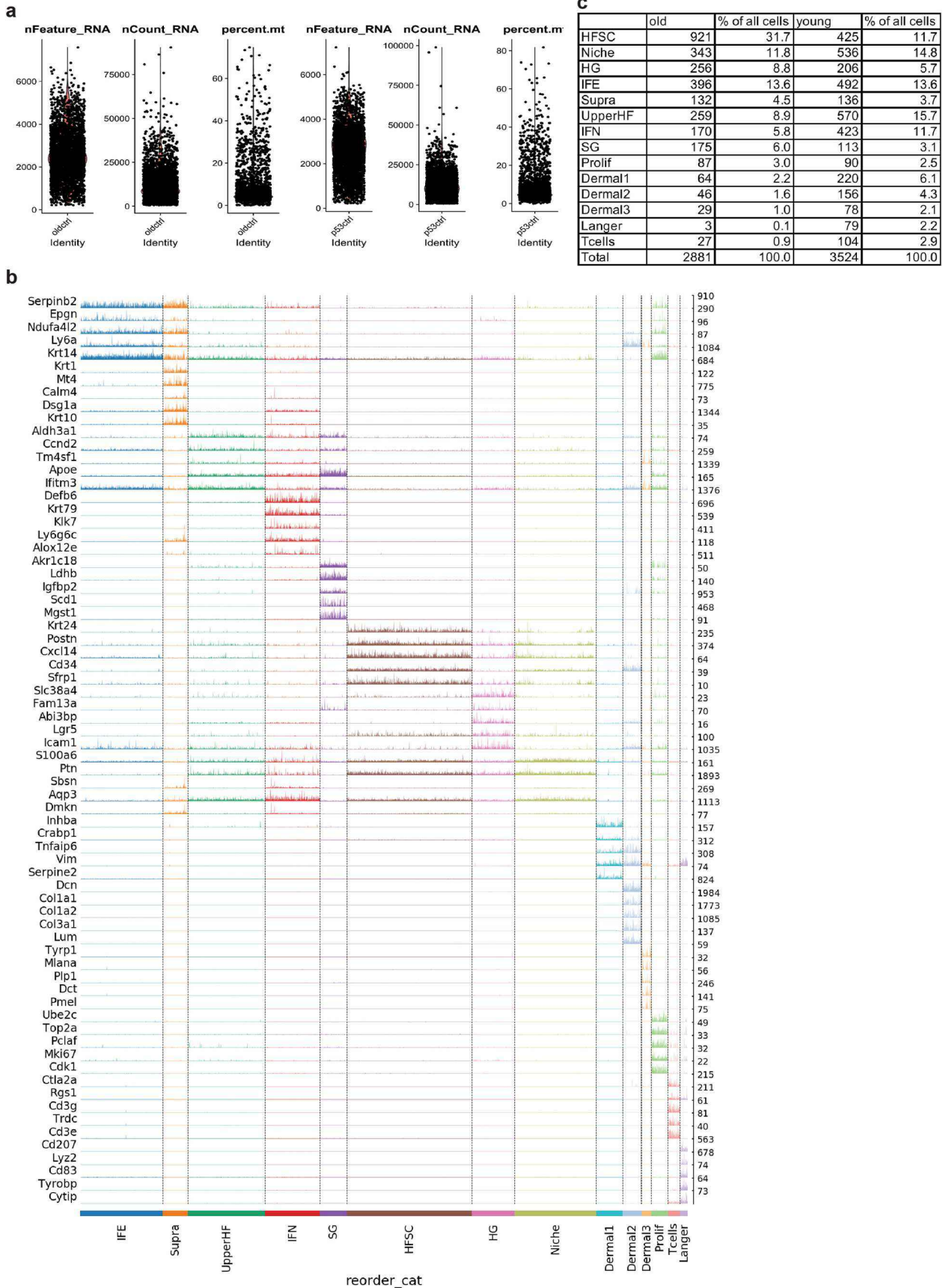
Publisher's note Springer Nature remains neutral with regard to jurisdictional claims in published maps and institutional affiliations.
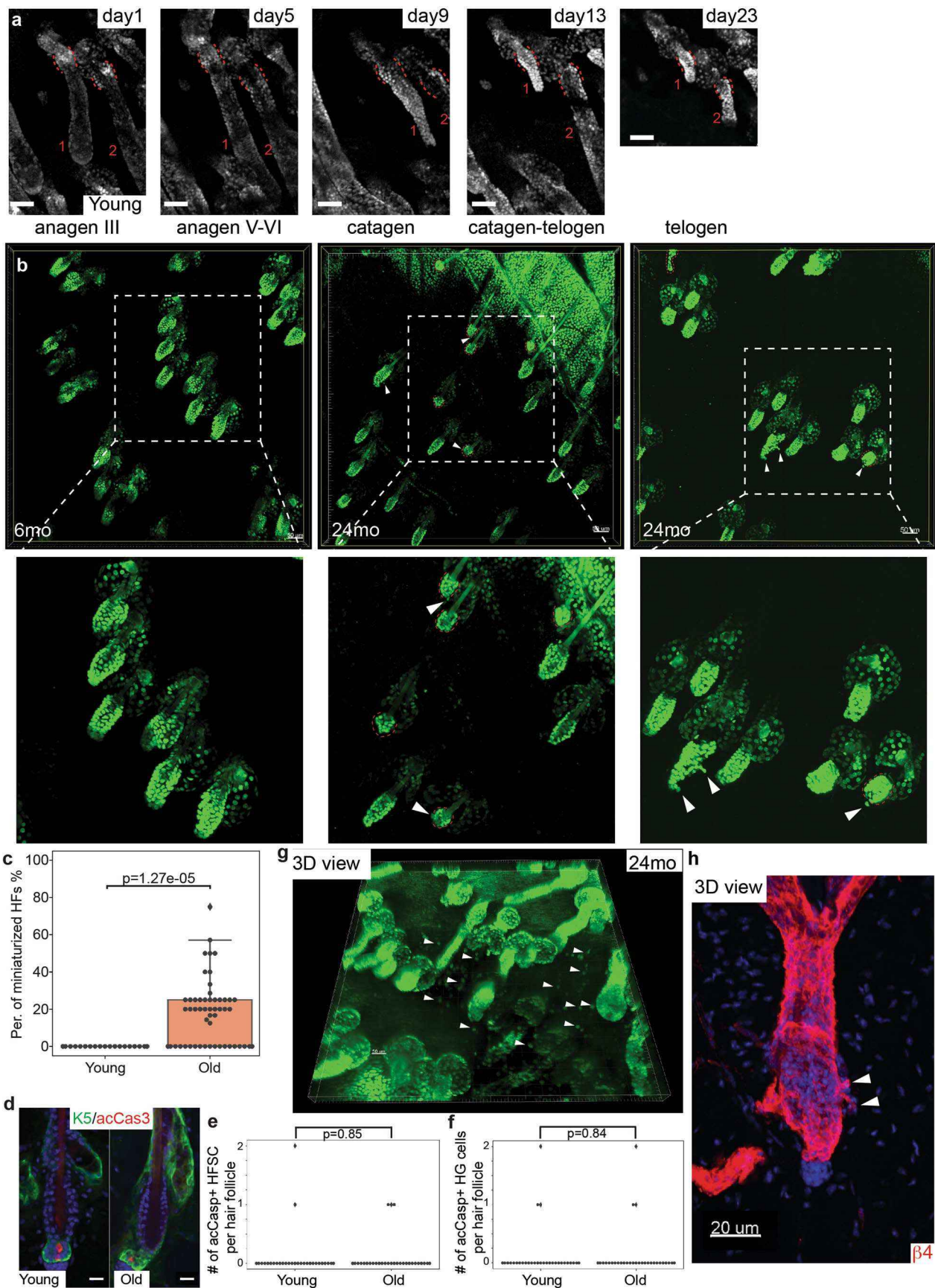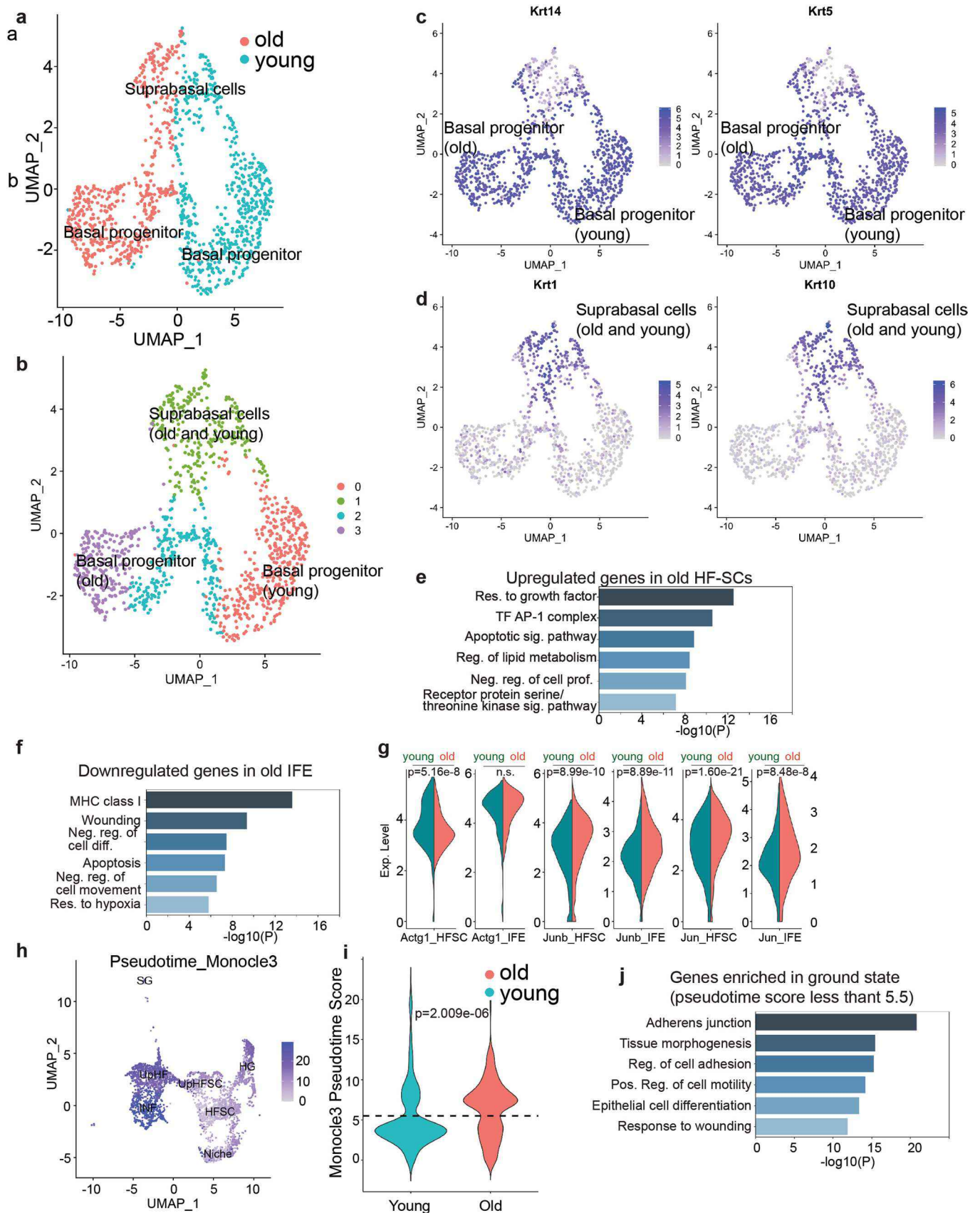
Extended Data Fig. 1 | See next page for caption.

Extended Data Fig. 1 | Live imaging of escaped cells in aging hair follicles. a, Two-photon longitudinal tracking of hair follicles in young mice during the anagen to telogen hair cycle. Red numbers designate the same hair follicle in each image. Red dotted lines annotate the bulge region. Scale bar, 50μm. **b**, Two-photon intravital imaging of hair follicles from young (left panel) and old (middle and right panels) mice. White arrowheads point to miniaturized hair follicles and cells located outside of the HF-SC compartments. Red dotted lines outline miniaturized hair follicles. Scale bar, 50μm. **c**, Boxplot of the percentage of miniaturized hair follicles, quantified from 3-D scan of live animals. (mean ± s.d.= 0 ± 0 (young), 14 ± 17 (old); n=205 HFs from 5 young mice; n=327 HFs from 3 old mice). **d**, Representative images of hair follicles with KRT5 and activated caspase 3 (acCas3) signals in young (6-8mo) and old (20mo) mice. (n=50 hair follicles from young mice; n=62 hair follicles from old mice, 3 pairs of mice). Scale bar, 20μm. **e-f**, Boxplot of number of acCas3+ HFSCs(e) and HG(f) per hair follicle (HFSCs: mean ± s.d.= 0.058 ± 0.31 (young), 0.048 ± 0.22 (old); HG: mean ± s.d.= 0.077 ± 0.33 (young), 0.065 ± 0.31 (old); n=50 hair follicles from young mice; n=62 hair follicles from old mice, 3 pairs of mice). **g**, 3-D view of hair follicles in 24mo old mice. White arrowheads point to numerous escaped epithelial cells scattering in the dermis. Scale bar, 50μm. **h**, 3-D view of β4 integrin immunofluorescence signals in 24mo old mice. White arrowheads point to HF-SCs with protruding integrin signals in the new bulge side. Scale bar, 20μm. Data in c, e, f are two-sided t-test.

a

b

c

	old	% of all cells	young	% of all cells
HFSC	921	31.7	425	11.7
Niche	343	11.8	536	14.8
HG	256	8.8	206	5.7
IFE	396	13.6	492	13.6
Supra	132	4.5	136	3.7
UpperHF	259	8.9	570	15.7
IFN	170	5.8	423	11.7
SG	175	6.0	113	3.1
Prolif	87	3.0	90	2.5
Dermal1	64	2.2	220	6.1
Dermal2	46	1.6	156	4.3
Dermal3	29	1.0	78	2.1
Langer	3	0.1	79	2.2
Tcells	27	0.9	104	2.9
Total	2881	100.0	3524	100.0

Extended Data Fig. 2 | See next page for caption.

Extended Data Fig. 2 | Quality control and clustering of single-cell RNA-seq data from young and old mice. a, Quality control and filtering of single cells from old and young samples. Cells were filtered with detected genes numbers (200<nFeature_RNA<5000), transcripts numbers (nCount_RNA) and mitochondrial percentage (percent.mt < 10). **b**, Track plot of marker genes for each cluster. **c**, Table shows cluster names, cell numbers and percentage of cells for each cluster after filtering of old and young scRNAseq data.
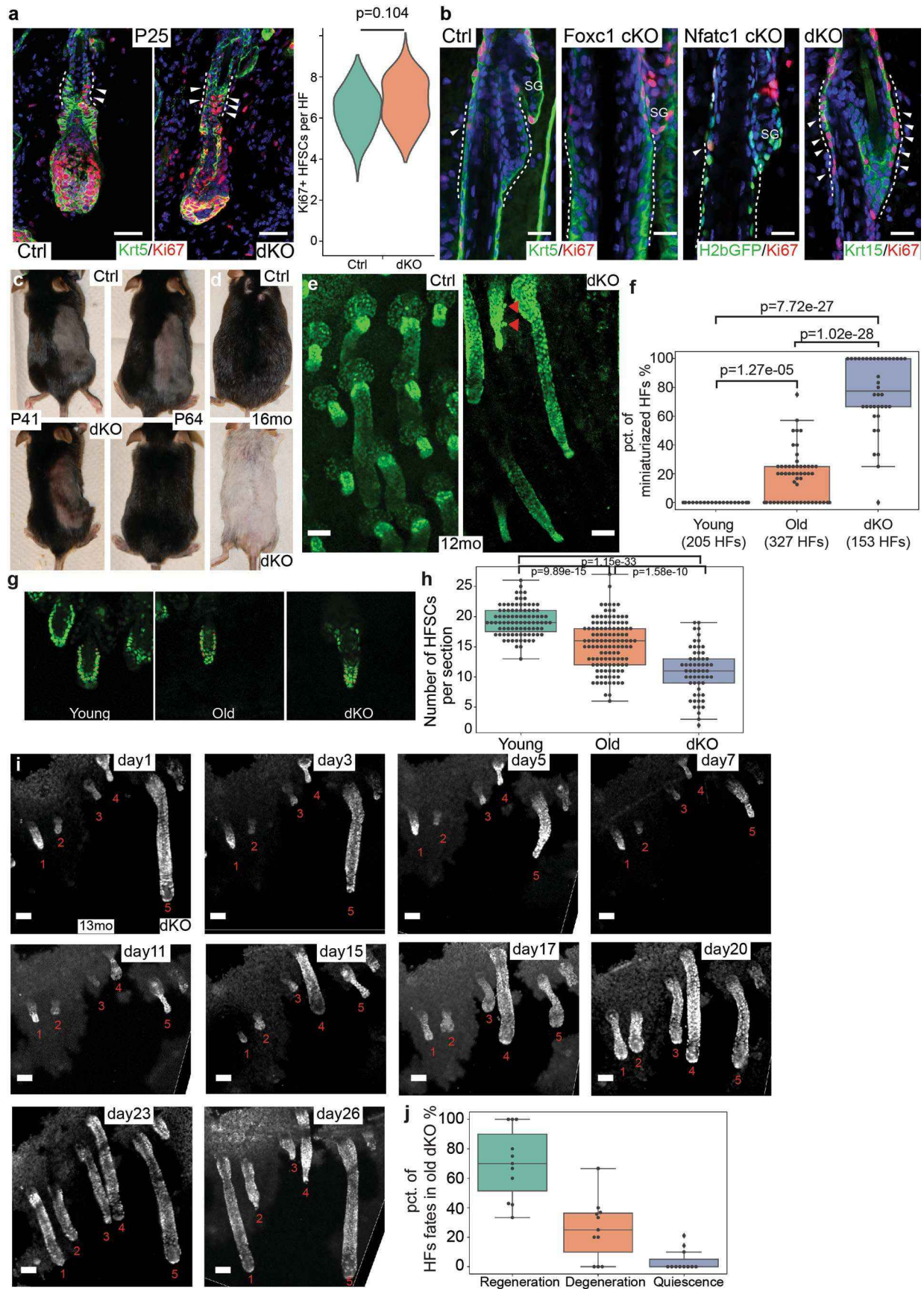
Extended Data Fig. 3 | See next page for caption.

Extended Data Fig. 3 | Single-cell transcriptomic analysis of old and young skin samples. a-b, UMAP re-clustering and projection of IFE cells, color coded by sample identity (**a**) and cluster identity (**b**). **c-d**, Feature plots of marker genes for basal progenitor cells (Krt14, Krt5) and suprabasal cells (Krt1, Krt10). **e-f**, Highly enriched GO terms for upregulated genes in old HFSCs (**e**) and downregulated genes in old IFE (**f**). **g**, Violin plots of selected gens in young and old HF-SC and IFE cell clusters. **h**, Feature plot of monocle3 pseudotime score of hair follicle cells from old and young mice. **i**, Violin plot of HFSCs pseudotime score in young and old samples. **j**, Highly enriched GO terms for HFSCs in the ground state with lower pseudotime score (<5.5).
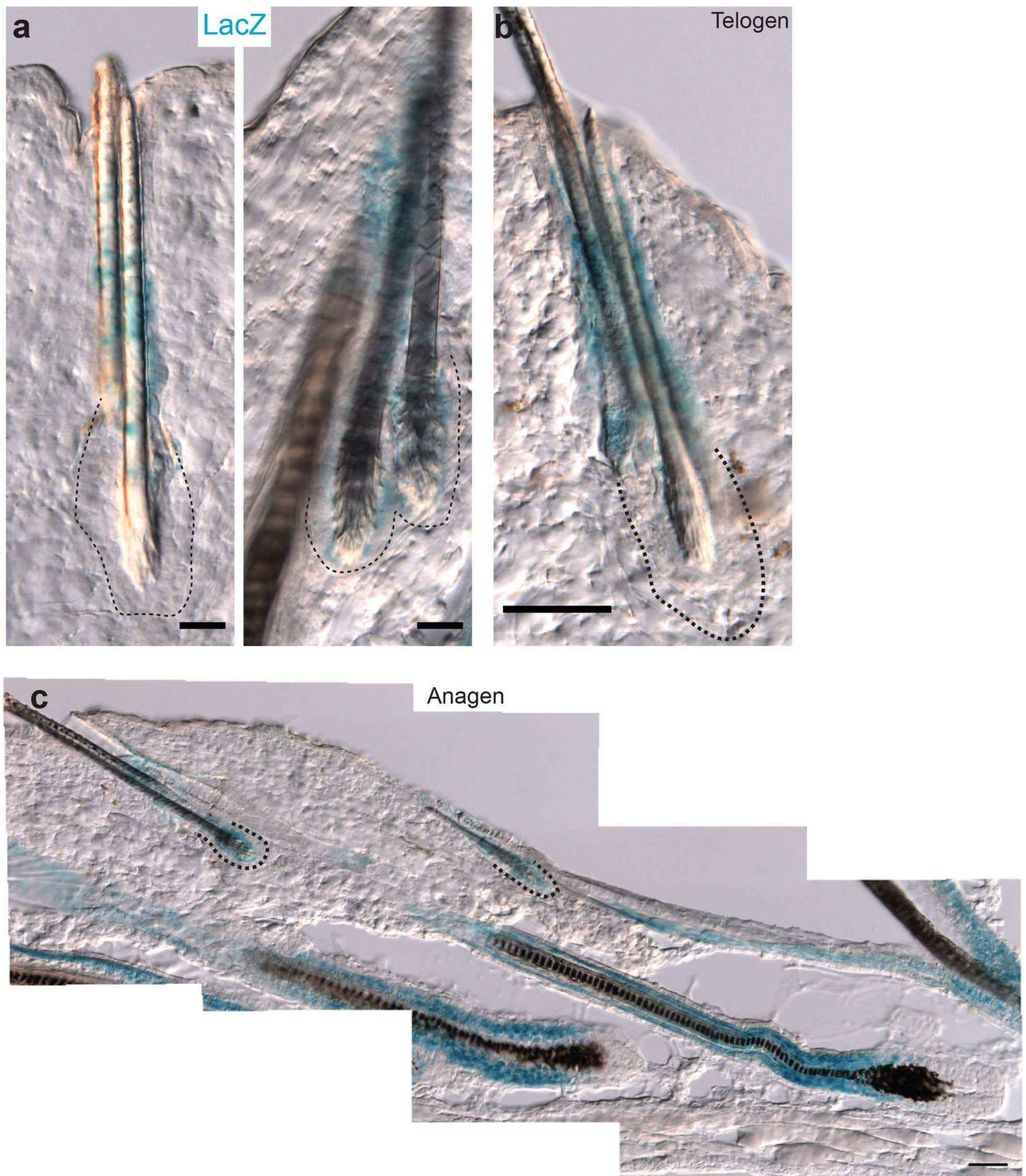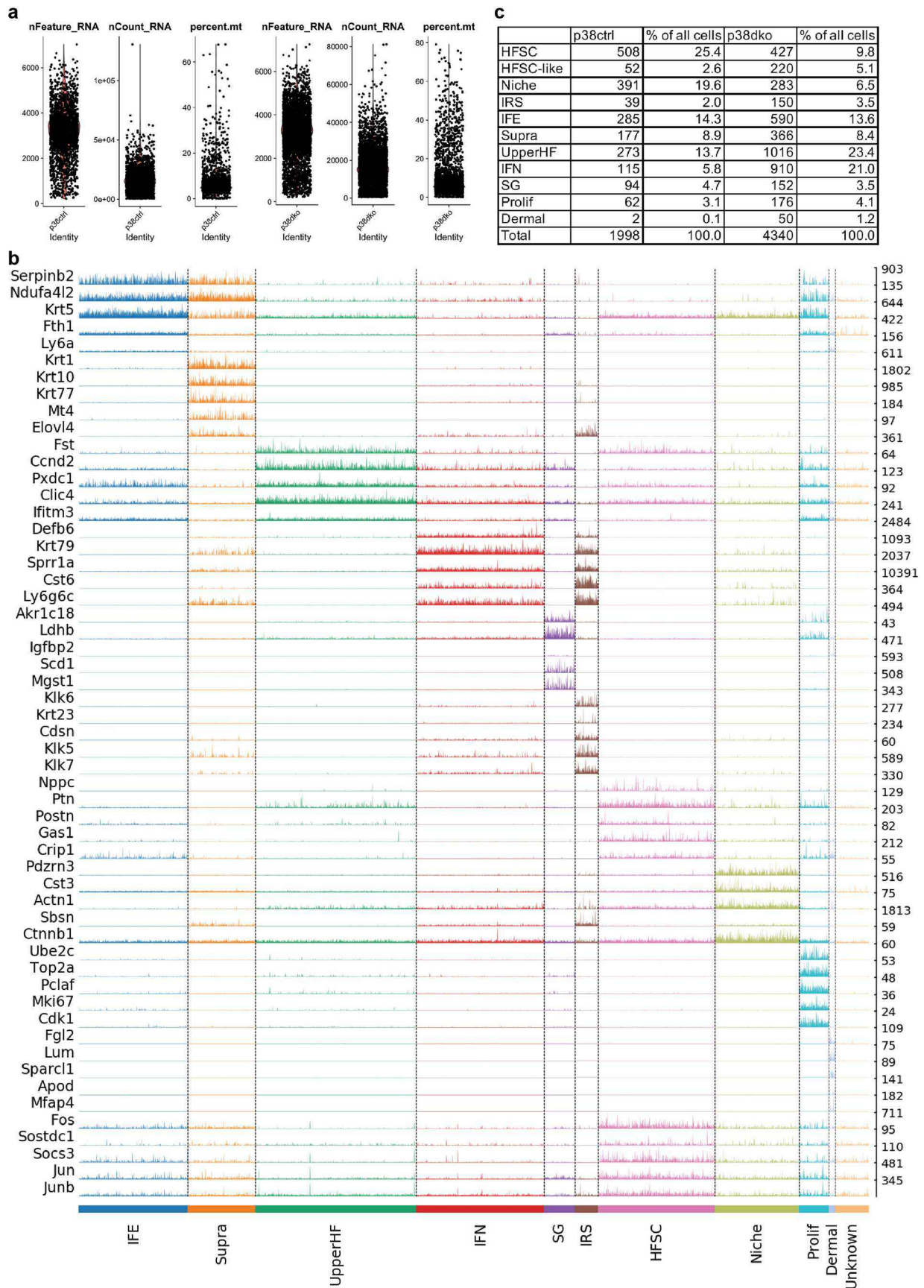
Extended Data Fig. 4 | Transcriptional activity of Foxc1 locus in 15mo old mouse skin. a, Transcriptional activity of *Foxc1* locus (*Foxc1-LacZ* knockin) is detected in anagen bulge but not detected in telogen bulge. Scale bar, 20μm. **b**, Transcriptional activity of *Foxc1* locus (*Foxc1-LacZ* knockin) is not detected in telogen bulge. Scale bar, 20μm. **c**, Robust transcriptional activity of *Foxc1* locus (*Foxc1-LacZ* knockin) is detected in both bulge and IRS regions of anagen hair follicles. Scale bar, 20μm.
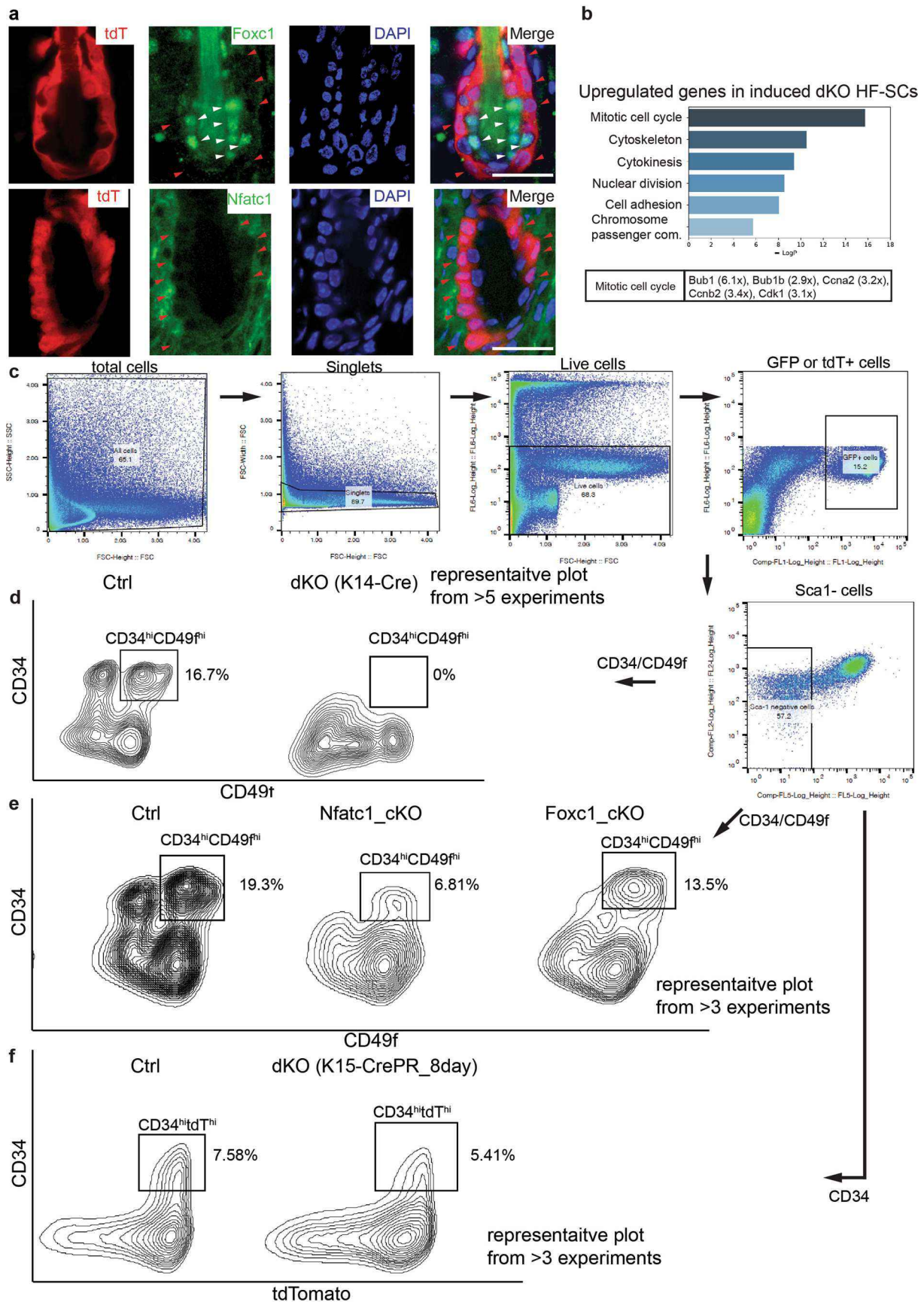
Extended Data Fig. 5 | See next page for caption.

Extended Data Fig. 5 | Hair follicle miniaturization and loss in dKO mice. a, Krt5 and Ki67 staining of hair follicles at early anagen (anagen III, P25) in control and dKO mice, arrowheads indicate Ki67+ HF-SCs, Right panel, quantification of Ki67+ HF-SCs per hair follicle (n=30 hair follicles from 3 pairs of mice). Scale bar, 20μm. **b**, Ki67 staining of hair follicles at late anagen (anagen V-VI) in control, *Foxc1* cKO, *Nfatc1* cKO, and dKO mice, arrowheads indicate Ki67+ HF-SCs. Scale bar, 20μm. **c**, Images of hair coat in the same control and dKO mice on P41 (left panel) and P64 (right panel), the right half of back skin was shaved on P41 and imaged again on P64. **d**, Images of hair coat of control and dKO mice at ~16mo old. **e**, Two-photon images of hair follicles in control and dKO mice at 12mo old, red arrowheads point to escaped cells outside of hair follicles. Scale bar, 70μm. **f**, Boxplot of the percentage of miniaturized hair follicles in young, old and dKO mice. (mean ± s.d.= 0 ± 0 (young), 14 ± 17 (old), 77 ± 25 (dKO); 5 young mice; 3 old mice; 5 dKO mice). **g**, Representative Two-Photon images for the quantification of HFSCs, red asterisks mark HFSCs(g). **h**, Boxplot of the number of HFSCs per HF in different samples. (mean ± s.d.= 19.33 ± 2.44 (young), 15.33 ± 4.04 (old), 10.95 ± 3.97 (dKO);91HFs, 5 young mice; 122 HFs, 3 old mice; 58 HFs, 5 dKO mice). **i**, Longitudinal tracking of dKO hair follicles over 26 days. Red numbers indicate the identical hair follicles in each image. Scale bar, 70μm. **j**, Boxplot of the percentage of HFs undergo regeneration, degeneration and quiescence in dKO samples (mean ± s.d.= 70 ± 24 (regeneration), 25.23 ± 25 (degeneration), 4.12 ± 7.49 (quiescence); 78 HFs from more than 3 mice were tracked for at least 16 days). Data in a, f, h are two-sided t-test.

a

c

|	p38ctrl	% of all cells	p38dko	% of all cells
HFSC	508	25.4	427	9.8
HFSC-like	52	2.6	220	5.1
Niche	391	19.6	283	6.5
IRS	39	2.0	150	3.5
IFE	285	14.3	590	13.6
Supra	177	8.9	366	8.4
UpperHF	273	13.7	1016	23.4
IFN	115	5.8	910	21.0
SG	94	4.7	152	3.5
Prolif	62	3.1	176	4.1
Dermal	2	0.1	50	1.2
Total	1998	100.0	4340	100.0

b

Extended Data Fig. 6 | See next page for caption.

Extended Data Fig. 6 | Quality control and clustering of single-cell RNA-seq data from control and dKO. a, Quality control and filtering of single cells from both control and dKO samples at P38. Cells were filtered with detected genes numbers (200<nFeature_RNA<5000), transcripts numbers (nCount_RNA) and mitochondrial percentage (percent.mt < 10). **b**, Track plot of marker genes for each cluster. **c**, Table shows cluster names, cell numbers and percentage of cells for each cluster after filtering of both control and dKO single-cell RNA-seq data.
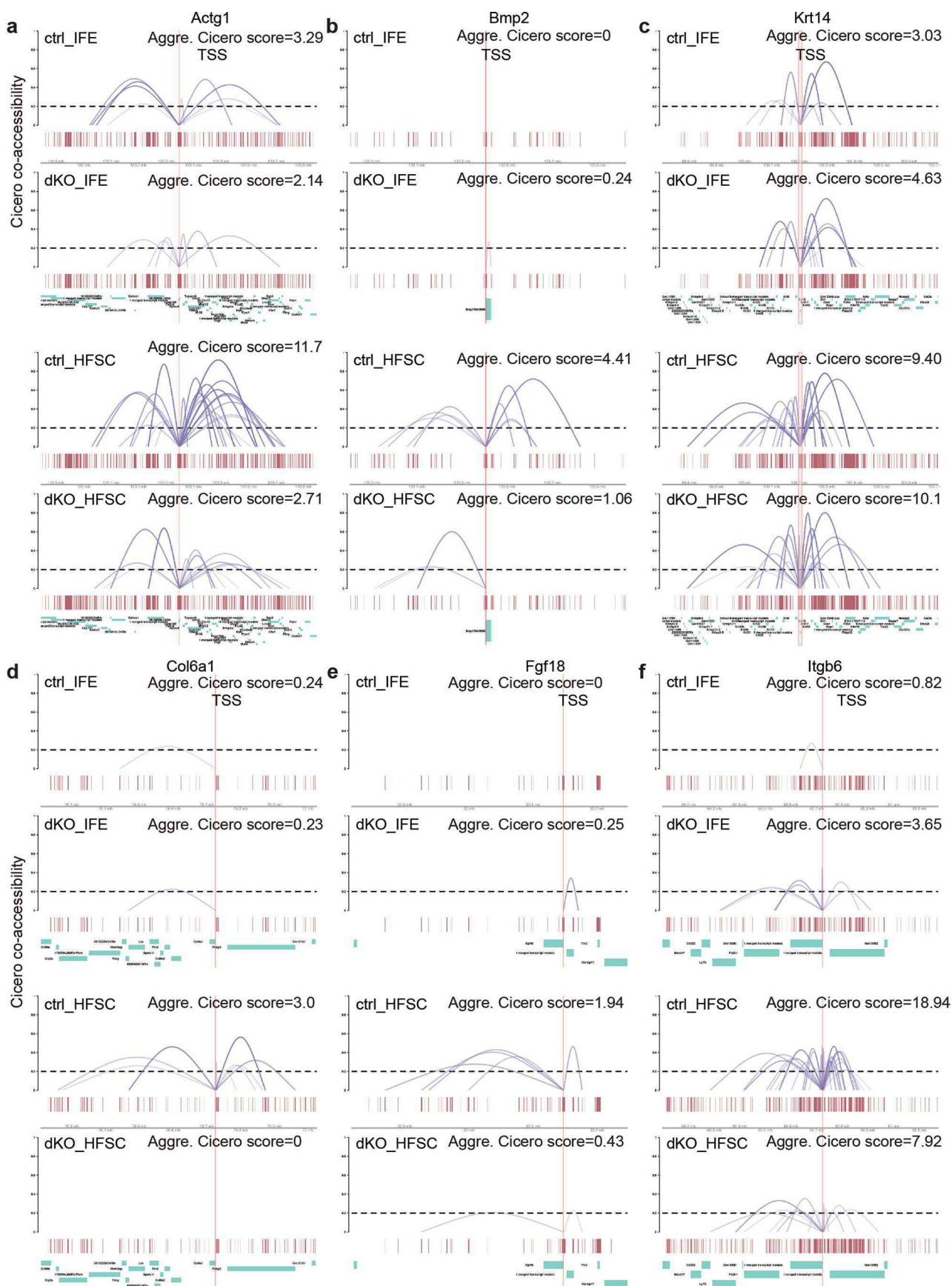
Extended Data Fig. 7 | See next page for caption.

Extended Data Fig. 7 | Isolation and transcriptomic analysis of Foxc1 and Nfatc1 single KO and induced dKO HF-SCs. a, Immunofluorescence staining of *Foxc1* and *Nfatc1* in *Krt15-CrePR* induced dKO hair follicles. tdT is tdTomato signals from *ROSA26-LSL-tdT* allele, indicating Cre+ dKO HF-SCs. Red arrowheads indicate HFSCs without *Foxc1* and *Nfatc1* signals, white arrowheads indicate inner bulge region, which is negative for tdT. Scale bar, 20μm. **b**, Highly enriched GO terms of upregulated genes and selected differentially expressed in induced dKO HF-SCs. **c**, Gating strategy for flow cytometry analysis. **d-f**, Flow cytometry analysis and quantification of HF-SCs during the first anagen (P28-P31) in control, Krt14-Cre-mediated dKO hair follicles (**d**), *Foxc1* cKO and *Nfatc1* cKO hair follicles (**e**). The rectangle regions are CD34-APC[hi] and Cd49f-PE [hi] HF-SC populations. Representative plots for 3~5 sets of experiments are shown. **f**, Flow cytometry analysis of Krt15-CrePR-mediated dKO hair follicles with *ROSA26-LSL-tdT* allele to mark Cre+ dKO cells. The rectangle regions are CD34-APC[hi] and tdTomato[hi] populations. Representative plots for 5 sets of experiments are shown.
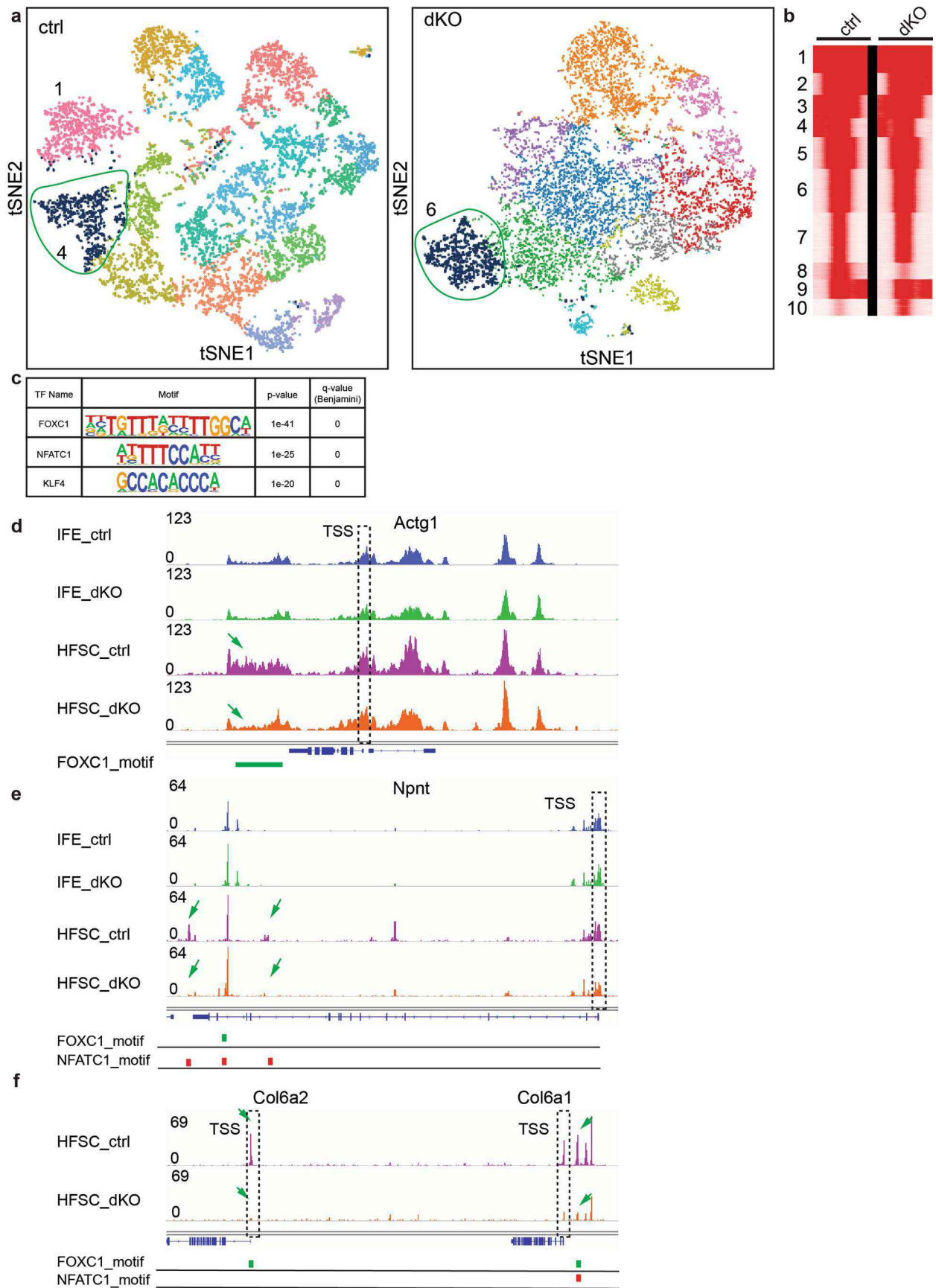
Extended Data Fig. 8 | See next page for caption.

Extended Data Fig. 8 | Single-cell ATAC analysis of Foxc1 and Nfatc1 controlled open chromatin in HF-SCs. a, tSNE plots of control and dKO total epithelial cells (Krt14-H2bGFP+). The HF-SC populations in each sample are highlighted in blue color and circled. The selected populations show the strongest open chromatin signatures of *Cd34*, the marker for HF-SC, and the weakest signatures of *Gata6*, a differentiation marker. **b**, K-means clustering of control and dKO open chromatin regions from aggregated scATAC-seq data from the HF-SC populations. Cluster 8 is reduced in dKO and cluster 10 is enhanced in dKO. **c**, Top 3 most highly enriched transcription factor motifs in cluster 8. **d-f**, Aggregated scATAC-seq tracks of *Actg1* (**d**), *Npnt* (**e**) and *Col6a1/2* (**f**) loci annotated with FOXC1 and NFATC1 motifs. Location of FOXC1 (green marks) and NFATC1 (red marks) motifs are indicated. Arrows point to HF-SC-specific open chromatin regions that are lost in dKO and the dashed rectangles mark the TSS of *Actg1, Npnt* and *Col6a1/2*, respectively.

Extended Data Fig. 9 | See next page for caption.

Extended Data Fig. 9 | Enhancer-promoter interactions are inferred by using aggregated Cicero scores computed from scATAC-seq. a-f, Enhancer-promoter interactions of *Actg1* (**a**), *Bmp2* (**b**), *Krt14* (**c**), *Col6a1* (**d**), *Fgf18* (**e**) and *Itgb6* (**f**) are illustrated in ctrl IFE, dKO IFE, ctrl HF-SC and dKO HF-SC. The aggregated Cicero score is calculated by the summation of Cicero scores of all enhancer-promoter interactions to the TSS region of each gene. The vertical lines mark the TSS and the dashed line indicates the cutoff of Cicero score (0.2) used for calculation.

a

b
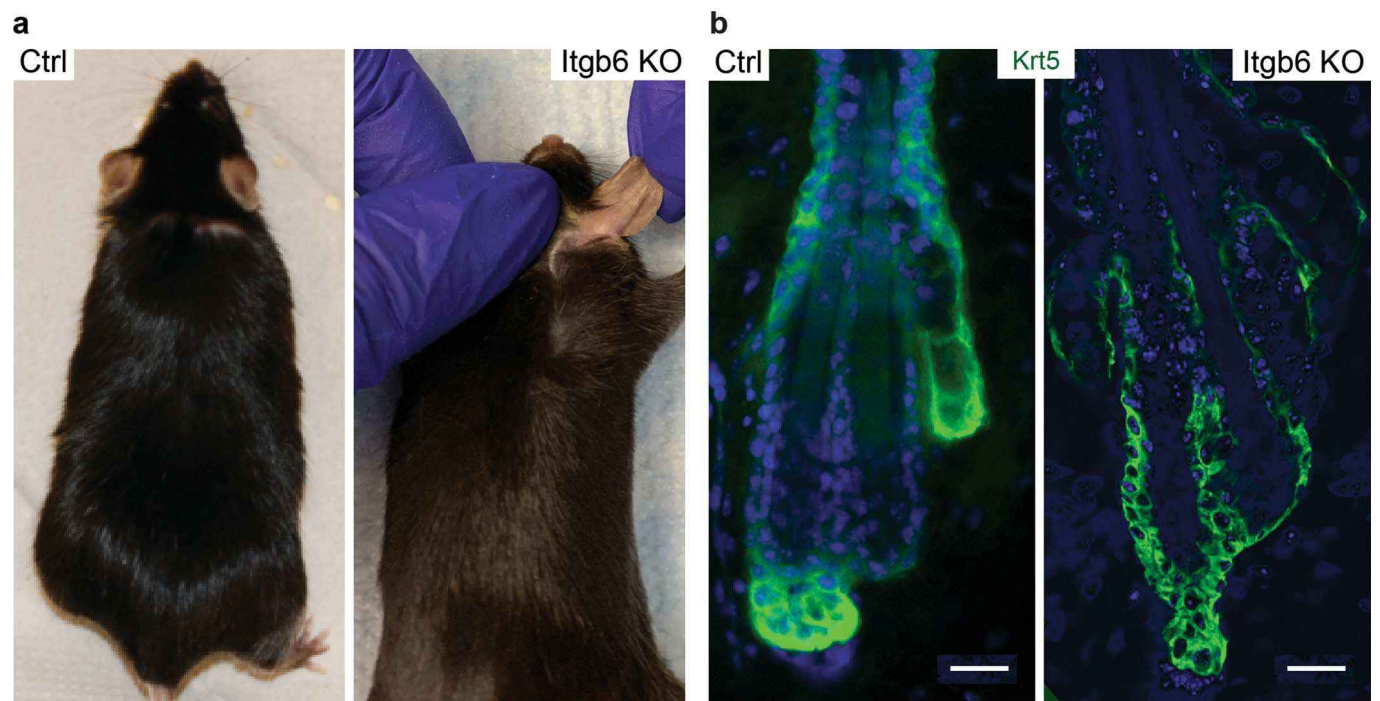
Extended Data Fig. 10 | Deletion of Itgb6 does not lead to premature hair loss. a, Hair coat is normal in both control and *Itgb6* KO animals at ~9-mo old. **b**, HF-SC compartment is normal in both control and *Itgb6* KO animals at ~9-mo old. Scale bar, 20μm.

nature research

Corresponding author(s): Rui Yi

Last updated by author(s): Jul 15, 2021

Reporting Summary

Nature Research wishes to improve the reproducibility of the work that we publish. This form provides structure for consistency and transparency in reporting. For further information on Nature Research policies, see our Editorial Policies and the Editorial Policy Checklist.

Statistics

For all statistical analyses, confirm that the following items are present in the figure legend, table legend, main text, or Methods section.

n/a	Confirmed	
☐	☒	The exact sample size (*n*) for each experimental group/condition, given as a discrete number and unit of measurement
☐	☒	A statement on whether measurements were taken from distinct samples or whether the same sample was measured repeatedly
☐	☒	The statistical test(s) used AND whether they are one- or two-sided *Only common tests should be described solely by name; describe more complex techniques in the Methods section.*
☐	☒	A description of all covariates tested
☐	☒	A description of any assumptions or corrections, such as tests of normality and adjustment for multiple comparisons
☐	☒	A full description of the statistical parameters including central tendency (e.g. means) or other basic estimates (e.g. regression coefficient) AND variation (e.g. standard deviation) or associated estimates of uncertainty (e.g. confidence intervals)
☐	☒	For null hypothesis testing, the test statistic (e.g. *F*, *t*, *r*) with confidence intervals, effect sizes, degrees of freedom and *P* value noted *Give P values as exact values whenever suitable.*
☒	☐	For Bayesian analysis, information on the choice of priors and Markov chain Monte Carlo settings
☒	☐	For hierarchical and complex designs, identification of the appropriate level for tests and full reporting of outcomes
☒	☐	Estimates of effect sizes (e.g. Cohen's *d*, Pearson's *r*), indicating how they were calculated

Our web collection on statistics for biologists contains articles on many of the points above.

Software and code

Policy information about availability of computer code

Data collection	Nikon NIS elements, Olympus FLUOVIEW software
Data analysis	The softwares are all public and detailed parameters are in methods session.

For manuscripts utilizing custom algorithms or software that are central to the research but not yet described in published literature, software must be made available to editors and reviewers. We strongly encourage code deposition in a community repository (e.g. GitHub). See the Nature Research guidelines for submitting code & software for further information.

Data

Policy information about availability of data

All manuscripts must include a data availability statement. This statement should provide the following information, where applicable:

- Accession codes, unique identifiers, or web links for publicly available datasets
- A list of figures that have associated raw data
- A description of any restrictions on data availability

All raw data for sequencing (scRNA-seq, RNA-seq, ATAC-seq and scATAC-seq) are deposited to NCBI/GEO.

Field-specific reporting

Please select the one below that is the best fit for your research. If you are not sure, read the appropriate sections before making your selection.

☒ Life sciences ☐ Behavioural & social sciences ☐ Ecological, evolutionary & environmental sciences

For a reference copy of the document with all sections, see nature.com/documents/nr-reporting-summary-flat.pdf

Life sciences study design

All studies must disclose on these points even when the disclosure is negative.

Sample size	No analysis was used to predetermine sample sizes.
Data exclusions	No data was excluded.
Replication	No attempts to replicate this data have been made outside of what is described in the paper.
Randomization	There was no allocation of samples into groups.
Blinding	No investigators were blinded for the analysis of this study.

Reporting for specific materials, systems and methods

We require information from authors about some types of materials, experimental systems and methods used in many studies. Here, indicate whether each material, system or method listed is relevant to your study. If you are not sure if a list item applies to your research, read the appropriate section before selecting a response.

Materials & experimental systems

n/a	Involved in the study
☐	☒ Antibodies
☒	☐ Eukaryotic cell lines
☒	☐ Palaeontology and archaeology
☐	☒ Animals and other organisms
☒	☐ Human research participants
☒	☐ Clinical data
☒	☐ Dual use research of concern

Methods

n/a	Involved in the study
☒	☐ ChIP-seq
☐	☒ Flow cytometry
☒	☐ MRI-based neuroimaging

Antibodies

Antibodies used	Primary antibodies (supplier; catalogue number; effective dilution) Chicken anti-Krt5 (BioLegend; 905901; 1:2000), mouse anti-Krt15 (Santa Cruz; sc-47697; 1:100), mouse anti-Nfatc1 (Santa Cruz; sc-7294; 1:100), rabbit anti-Foxc1 (Cell Signaling; #8758; 1:500), rabbit anti-Sox9 (Millipore Sigma; AB5535; 1:500), rabbit anti-Periostin (Abcam; ab14041; 1:500), rabbit anti-Lhx2 (gift from E. Fuchs; 1:2000), rabbit anti-NPNT (gift from H. Fujiwara; 1:500), rabbit anti-EGFL6 (gift from H. Fujiwara; 1:500), rabbit anti-Ki67 (Abcam; ab15580; 1:500), rat anti-ECad (gift from E. Fuchs; 1:200), rat anti-CD34 (eBiosciences; 14-0341-85; 1:500) Secondary antibodies (supplier; catalogue number; all used at 1:1000) Anti-chicken-Alexa 594 (Invitrogen; A-11042), anti-chicken-Alexa 488(Invitrogen; A-11039), anti-mouseIgG1-Alexa 488(Invitrogen; A-21121), anti-mouseIgG1-Alexa 647(Invitrogen; A-21240), anti-mouseIgG2a-Alexa 594(Invitrogen; A-21135), anti-rabbit-Alexa 488(Invitrogen; A-21206), anti-rabbit-Alexa 555(Invitrogen; A-21428), anti-rabbit-Alexa 647(Invitrogen; A-21244), anti-rat-Alexa 488(Invitrogen; A-21208), anti-rat-DyLight 549(Jackson ImmunoResearch; 712-505-153)
Validation	Antibodies were validated with previous publication in the Yi lab.

Animals and other organisms

Policy information about studies involving animals; ARRIVE guidelines recommended for reporting animal research

Laboratory animals	Mus musculus
Wild animals	N/A

Field-collected samples	N/A
Ethics oversight	The animal protocol is approved by the IACUC at University of Colorado Boulder and Northwestern University, respectively.

Note that full information on the approval of the study protocol must also be provided in the manuscript.

Flow Cytometry

Plots

Confirm that:

☒ The axis labels state the marker and fluorochrome used (e.g. CD4-FITC).

☒ The axis scales are clearly visible. Include numbers along axes only for bottom left plot of group (a 'group' is an analysis of identical markers).

☒ All plots are contour plots with outliers or pseudocolor plots.

☒ A numerical value for number of cells or percentage (with statistics) is provided.

Methodology

Sample preparation	Gender and hair cycle matched anagen mice were euthanized and collected for dissection right after. We first shave the hair coat and then apply nair hair removal lotion(amazon, 22339) for around 3 minutes. After wipe off the lotion and wash away leftover hair shaft, back skin was dissected and subcutaneous fat was removed using a blade. Small part of the skin sample was embedded in OCT and the remaining skin sample was minced and incubated with 0.25% collagenase(Worthington, LS004188) in 4-6mL 1x HBSS buffer at 37℃ for 2 hours with rotation. Use 5mL serological pipet to further separate epidermis from dermis at 1hour incubation time. After collagen treatment, add 10mL cold PBS to the sample and transfer to 50mL conical tube. Centrifuge at 400g for 10minutes at 4 °C. Remove the supernatant carefully and resuspend the pellet with pre-warmed 0.25% trypsin/EDTA(Gibco) for 8minutes at 37°C and immediately transfer 10mL cold 1xPBS with 3% chelated FBS. The suspension was extensively triturated with a 10ml pipette and passed over a 40um cell strainer. Centrifuge for 5 minutes at 4°C to pellet cells and resuspend cells in cold 1xPBS with 3% chelated FBS. Cells were incubated with appropriated antibodies for 1 hour on ice. DAPI was used to exclude dead cells.
Instrument	FACS was performed on MoFlo XDP machine (Beckman Coulter).
Software	FACS data were analyzed with FlowJo.
Cell population abundance	*Describe the abundance of the relevant cell populations within post-sort fractions, providing details on the purity of the samples and how it was determined.*
Gating strategy	Hair follicle stem cells of K14Cre based experiments were isolated by enriching DAPIneg, K14-H2BGFPhi, Sca1lo, α6hi and CD34hi cells. HFSCs of K15CrePR- based experiments were isolated by enriching DAPIneg, K14-H2BGFPhi , tdtomatohi, Sca1lo and CD34hi cells. The following antibodies were used: integrin α6 (CD49f, 1:75; eBioscience, PE-conjugated, 12-0495; APC-conjugated, 17-0495), CD34 (1:50; eBioscience, eFluor 660-conjugated, 50-0341), Sca1 (Ly-6A/E, 1:500; eBiosciences, PerCP-Cy5.5-conjugated, 45-5981).

☐ Tick this box to confirm that a figure exemplifying the gating strategy is provided in the Supplementary Information.